Doctoral Thesis

Enhancement of Practical Energy Product by Mircostructure Modeling

Namkyu Kim

Department of Materials Science and Engineering

Ulsan National Institute of Science and Technology

2021

Enhancement of Practical Energy Product by Mircostructure Modeling

Namkyu Kim

Department of Materials Science and Engineering

Ulsan National Institute of Science and Technology

Enhancement of Practical Energy Product by Mircostructure Modeling

A thesis/dissertation submitted to
Ulsan National Institute of Science and Technology
in partial fulfillment of the
requirements for the degree of
Doctor of Philosophy

Namkyu Kim

12/21/2020 of submission

Approved by

Advisor
Ki-Suk Lee

Enhancement of Practical Energy Product by Mircostructure Modeling

Namkyu Kim

This certifies that the thesis/dissertation of Namkyu Kim is approved.

12/21/2020 of submission

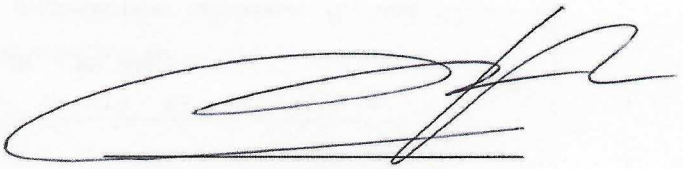

Advisor: Ki-Suk Lee

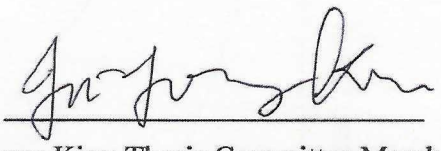

Ju-Young Kim: Thesis Committee Member #1

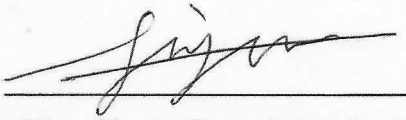

Jiyun Kim: Thesis Committee Member #2

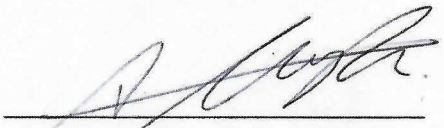

Hungson Son: Thesis Committee Member #3

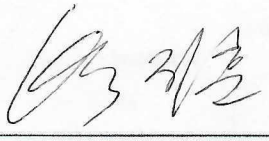

Jihoon Park: Thesis Committee Member #4

Abstract

Devices such as electric vehicles and wind power generators utilize the magnetic energy of permanent magnet. To meet the increasing demand for such devices, researchers have actively developed permanent magnets with higher efficiencies and lower cost. Magnetic energy is represented by the energy product *BH*, which is twice the energy stored in the stray field outside the magnet. It can be obtained from the volume integral of the square of the stray field outside the magnet, or from the volume integral of the dot product between the demagnetizing field H_d and the internal magnetic flux density *B*. The maximum energy product, $(BH)_{max}$ is widely used as a figure of merit for evaluating the performance of hard-magnetic materials. $(BH)_{max}$ should be evaluated rigorously from the hysteresis loop by considering the exact working point, which is determined by the shape of the magnet. However, many researchers still use $(BH)_{max}$ obtained from the hysteresis loop of a certain shape as a representation of the material, even though the only information *BH* from a certain shape of the magnet is an energy product at the remanent state. Thus, correctly calculated $(BH)_{max}$ was compared with that of obtained from conventional way through several models by using micromagnetic simulation.

To obtain high energy product for permanent magnet, high saturation magnetization and coercivity is essential. However, there is still large discrepancy between theory and practice. This clear contradiction is called Brown's paradox. One of the main reasons for the paradox is known as microstructure including grain properties, grain boundary, crystalline anisotropy distribution, and so on. Despite this importance, the effect of microstructure on magnetic properties have not much been studied. Thus, the effect of various microstructure has been discussed by theoretical and numerical methods, and then the microstructures having high energy product are proposed. Furthermore, cylindrical core/shell exchange-coupled magnet having diverse conditions by microstructure modeling has been investigated.

Contents

List of Figures

List of Tables

1. Introduction

1.1 Permanent Magnet

Devices such as electric vehicles and wind power generators utilize the magnetic energy of permanent magnet. To meet the increasing demand for such devices, researchers have actively developed permanent magnets with higher efficiencies and lower cost [1]–[8]. Nonetheless how strong magnetic field emitted is important, it is hard to measure the magnetostatic energy from magnetic field distributed in free space. Hence, the performance of permanent magnet is epitomized by the energy product, which is equal to twice the magnetostatic energy stored in free space divided by the volume of the magnet. It can be obtained from the volume integral of the square of the stray field outside the magnet, or from the volume integral of the dot product between the demagnetizing field H_d and the internal magnetic flux density B. Especially, the maximum energy product, $(BH)_{max}$ is widely used as a figure of merit for evaluating the performance of hard-magnetic materials. $(BH)_{max}$ should be evaluated rigorously from the hysteresis loop by considering the exact working point, which is determined by the shape of the magnet. However, many researchers still use $(BH)_{max}$ obtained from the hysteresis loop of a certain shape as a representation of the material, even though the only information BH from a certain shape of the magnet is an energy product at the remanent state. Thus, correctly calculated $(BH)_{max}$ was compared with that of obtained from conventional way through several models by using micromagnetic simulation.

To obtain high energy product for permanent magnet, high saturation magnetization and coercivity is essential. However, there is still large discrepancy between theory and practice [9]. This clear contradiction is called Brown's paradox (Figure 1.1). The coercivity is essential for attaining theoretical maximum energy product, nonetheless there is no direct contribution for energy product to the coercivity. Unlike the intrinsic properties for permanent magnet, the coercivity is largely affected by the microstructure of the magnetic system. Of course, the anisotropy field is determined by magnetocrystalline anisotropy energy of the magnet. To make a better permanent magnet, it seems essential to design and control the microstructure. However, the microstructure is too complicated to make simplified model and had not been theoretically well established. In recent year, it is possible to study complicated microstructure by development of computing technology, and many researchers had been investigated microstructure properties of magnet. But the study for the microstructure still has a bunch of problems to solve. In this thesis, I tried to set the correct theory for the effect of the microstructure on the magnetic properties for permanent magnet up by combination of micromagnetic simulation and analytic solver.

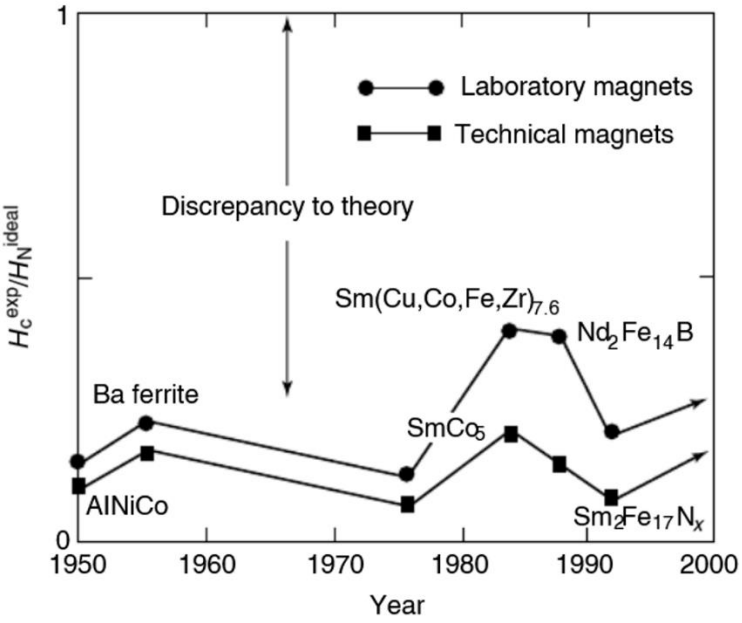

Figure 1.1 Brown's paradox: The experimentally realized coercivities amount to a factor of 3 – 5 smaller than the ideal nucleation field [9].

1.2 Motivation

To decrease the discrepancy between theoretical anisotropy field H_A and experimentally measured coercivity, the study for the microstructure must be carried out. At first, I tried to set the correct theory for understanding the physics of the magnet. Even if the energy product is important figure-of-merit to estimate the magnetic materials, the physical meaning of the energy product has been overlooked due to an experimental limit such as hardness measuring the internal magnetic field. Thus, I will cover the detailed theoretical background for the permanent magnet, the reason what determines the energy product of a magnet, why coercivity is important.

Next, through an understanding of the microstructure of the magnets, the models for investigating the effect of the microstructure on the magnetic properties for the permanent magnet is established and calculated by micromagnetic solver [10]. In order to simulate the correct system, underlying physics is considered to the model system, which is critical factor such as the exchange length, singe domain size, the degree of grain anisotropy alignment, and so on. By maximizing the advantages of the micromagnetic simulation, various physical quantities are studied from the simulated model structure. In spite of the importance of these physical quantities, it is not easy to obtain through experiments. In this thesis, the microstructure characteristics of magnets were analyzed and the basis for designing an optimized structure was established through these physical quantities' analysis.

To develop the magnet having high energy product, exchange-coupled magnet is proposed, which combines the high coercivity of the hard magnet with the high saturation magnetization of the soft magnet. Since an exchange-coupled magnet is a magnet utilizing quantum mechanical exchange interaction that affects a short distance (~nm), the ratio of the material in the magnet and interfacial properties have a great influence on the magnetic properties of the entire magnet. From the studies via micromagnetic simulation, the elaborately designed structures can be investigated and the optimized structures for the exchange-coupled magnet can be suggested.

2. Theoretical Development

2.1 Micromagnetic Energy

Magnetic System is to be sure to follow a result of minimizing the total free energy, which means the system is stabilized at a local or absolute energy minimum. Magnetic energy density is consisted of many energy terms [11], [12]. But here I cover four main energy terms for magnetic system.

$$E = E_{\text{exc}} + E_{\text{ani}} + E_{\text{demag}} + E_{\text{Zeeman}}$$

The first term comes from exchange interaction, which is originated by quantum mechanical interference between wave function of two electrons. The exchange energy is one of the powerful energies for making magnetic arrangement, and expressed as

$$E_{\text{exc}} = -J_{ij} S_i \cdot S_j$$

where J_{ij} is the exchange constant between S_i and S_j, which affecting alignment of neighboring spin moments. Positive value of the exchange constant makes the spin moments heading same direction, which results in the phenomenon of long-range magnetic order.

The energy of a magnet depends on the direction of the magnetization with respect to the crystal axes. This property comes known as the magnetic anisotropy is the origin of hysteresis and coercivity of the magnet, and the anisotropy energy is most important energy for permanent magnet determining its anisotropy field. The value of this anisotropy energy classifies soft magnetic materials and hard magnetic materials. Since the difference between energy by direction is large, the materials having uniaxial anisotropy energy is used for permanent magnet, and the uniaxial anisotropy energy density is represented on below equation.

$$E_{\text{ani}} = K_1 \sin^2\theta + K_2 \sin^4\theta + K_3 \sin^6\theta$$

Where K_1, K_2, and K_3 are the first, second, and third uniaxial anisotropy constants, respectively. The exchange length, which is the length scale where the magnetization changes smoothly without strong inhomogeneity, is calculated by competition between this anisotropy energy and the exchange stiffness.

$$l_{ex,K_1} = \sqrt{\frac{A}{K_1}}$$

In the case of hard magnet, the exchange length calculated from the uniaxial anisotropy energy is usually smaller than the exchange length calculated from the saturation magnetization.

The third energy term is demagnetizing energy, which is originated from the magnetostatic interaction of a pair of magnetic dipoles. The demagnetizing energy is related with the shape of the magnet. To decrease the energy from interaction between dipoles, the demagnetizing energy is minimized at needle-like shape magnets and maximized at plate-like shape magnets, and the energy follows the equation

below.

$$E_{\text{demag}} = -\frac{1}{2}\mu_0 M \cdot H_d$$

Where H_d is the demagnetizing field inside the magnet.

Finally, Zeeman energy is considered for micromagnetic simulation of the magnetic system. Zeeman energy is the potential energy of a magnet in the external magnetic field and expressed like next equation.

$$E_{\text{Zeeman}} = \mu_0 M \cdot H_{\text{app}}$$

Where H_{app} is the external magnetic field.

Most of magnetic phenomena including magnetic hysteresis, domain wall, and so on, are originated from the combination of these four energy terms.

2.2 Stoner-Wohlfarth Model

To calculate the hysteresis loop for ferromagnetic materials, there is very popular and powerful model known as Stoner-Wohlfarth model [13]–[15], which was proposed in 1948. The model firstly assumes a single magnetic particle having parallel spin alignment, which means that the spin moments rotate coherently without the generation of domain wall. In addition, the exchange energy is considered as constant, not involving in energy minimization. The demagnetizing energy is also neglected in Stoner-Wohlfarth model. There are then only uniaxial crystalline anisotropy energy and Zeeman energy from interaction between magnetic moments and the applied magnetic field to be considered. Figure 2.2 shows a schematic image of a Stoner-Wohlfarth particle for the model.

As mentioned in previous paragraph, the total energy density of the system is composed of uniaxial anisotropy energy from an angle difference, $(\omega-\theta)$, between direction of the easy axis of the magnetic system and that of the magnetization, *M*, and Zeeman energy from the angle difference, θ, between the direction of the magnetization and that of the applied magnetic field, H_{app}, which is expressed below.

$$\frac{E}{V} = K_1 \sin^2(\omega-\theta) - \mu_0 H M_s \cos\theta$$

The energy density can be minimized to find the direction of the magnetization at given applied magnetic field, and the direction of the magnetization results in a magnetic hysteresis loop along the direction of the applied field. The equation is normalized to dimensionless equation by using a parameter *h*, which is represented by

$$h = \frac{\mu_0 M_s H_{app}}{2K_1}$$

and the converted energy density equation is expressed below.

$$\varepsilon = \frac{E}{2K_1 V} = \frac{1}{2}\sin(\omega-\theta) - h\cos\theta$$

For given values of ω and *h*, the magnetization will choose the angle, θ, which minimizes the energy density, and the solution is expressed as

$$\frac{\partial\varepsilon}{\partial\theta} = -\sin(\omega-\theta)\cos(\omega-\theta) + h\sin\theta = 0$$

Because the above solution alone cannot distinguish whether the energy is minimum or maximum, the second derivative of the energy density should be larger than zero.

$$\frac{\partial^2\varepsilon}{\partial\theta^2} = \cos^2(\omega-\theta) - \sin^2(\omega-\theta) + h\cos\theta > 0$$

Figure 2.1 shows representative hysteresis loop calculated from energy density with increasing field magnitude, where the Stoner-Wohlfarth particle in the applied field along the angle $\omega = \pi / 5$ with the easy axis. When the applied field gradually changes from large negative value to large positive value, multiple minima at several angle appear and disappear. For instance, energy minimum at $h = -0.7$ becomes shallow with the increase of the applied magnetic field, and it is expressed in Figure 2.1 (a). When h becomes -0.46, another minimum point appears at certain angle. With continuous increase the applied field, new energy minimum has lower energy density than former minimum. However, energy barrier between energy minima interrupts energy transition to lower energy, and this is the origin of hysteresis. After the local energy minimum disappears, energy transition to global minimum occurs. The stable states are expressed with colored circle, and the angle θ at local energy minimum results in the magnetization with $M = M_s \cos\theta$. Finally, the Stoner-Wohlfarth hysteresis loop comes out in Figure 2.1 (b). From this way, the magnetization in applied field direction for various angles ω is shown in Figure 2.3. For $\omega = 0$, the model shows a perfect square loop whose coercivity is equal to the anisotropy field $H_a = 2K_1 / \mu_0 M_s$. For hard axis loop, where ω is $\pi / 2$, the magnetization is linearly increased by the increase of external magnetic field. In other words, the magnetization of the case is proportional to the applied magnetic field with zero coercivity and saturated at $h = \pm 1$.

Most powerful point of this theory is so simple to add some extra features easily on the model. Thus, models considering second order anisotropy term and anisotropy distribution of nanostructure will be covered in later chapter.

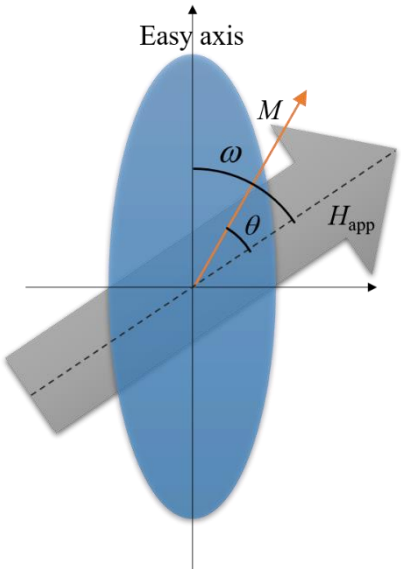

Figure 2.2 A Stoner-Wohlfarth particle

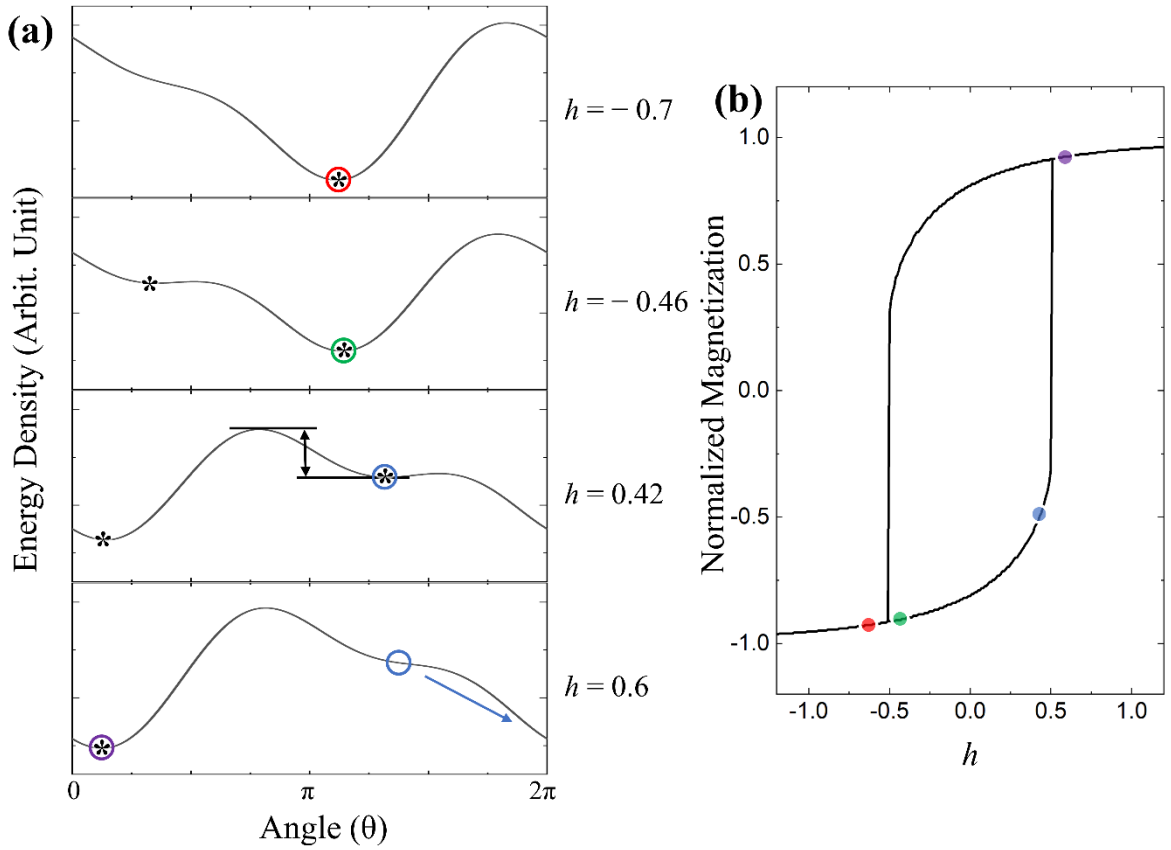

Figure 2.1 (a) Energy density of Stoner-Wohlfarth model with the change of the angle, θ, where the external field is applied with the angle(ω) of $\pi/5$. (b) Magnetic hysteresis loop calculated from energy density, and the color-filled circle means the magnetization of same colored circle in energy density.

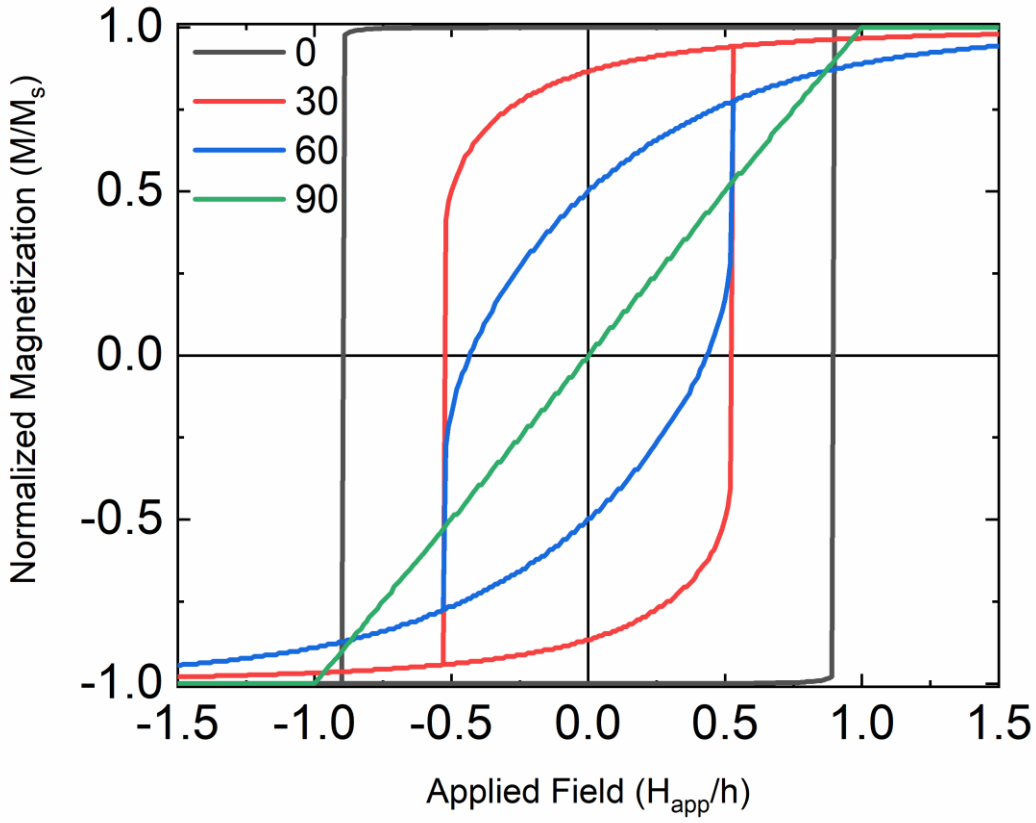

Figure 2.3 Stoner-Wohlfarth Magnetic hysteresis loops as a function of normalized magnetization and applied magnetic field. The loops are calculated by the change of angle between the easy axis and the applied field direction.

2.3 Magnetic Hysteresis

In general, spontaneous magnetization of a ferromagnetic materials exhibits different hysteresis characteristics depending on the direction of the applied magnetic field. This property is measured like magnetic hysteresis loops shown in Figure 2.4. As shown in Figure 2.4 (b), various physical quantities related to magnetism, magnetic moment (*M*) and magnetic flux density (*B* magnetic field, *B*-field) or magnetic field strength (*H* magnetic field, *H*-field), and the hysteresis curve can be converted into several physical quantities from their relationship, which will be introduced next.

In free space, *B*-field vector and *H*-field vector have a relation like below.

$$\boldsymbol{B} = \mu_0 \boldsymbol{H}$$

B-field also includes magnetization (*M*) in the magnet having magnetic moments and expressed below.

$$\boldsymbol{B} = \mu_0 \left(\boldsymbol{H} + \boldsymbol{M} \right)$$

Where μ_0 is the magnetic permeability. In addition, *H*-field inside the magnet can be classified into eternally applied magnetic field (H_{app}) and demagnetizing field emitted by magnetization (*M*). Because the demagnetizing field generated inside the magnet is hard to measure by experiment, the demagnetizing field should be theoretically calculated. If the magnetic moments inside the magnet are coherent, the demagnetizing field can be expressed using tensor ($\mathbb{N}$).

$$H_d = -\mathbb{N}M$$

The demagnetizing tensor is determined by the shape of the magnetic body, and in typical structures such as sphere, ellipsoids, and thin film, the demagnetizing tensor can be expressed by approximating the demagnetizing factor (*N*) as a constant as shown below.

$$H_d \approx -NM$$

Here, the demagnetizing factor (*N*) varies depending on the shape of the magnet and the direction of the magnetic moments. For instance, in the case of a sphere, since it is symmetric in all directions, $N = 1/3$ regardless of the direction. On the other hands, in the case of a thin film, *N* is to be 1 along the perpendicular direction to the thin film plane, and $N = 0$ if it is parallel to the thin film plane. In the case of a cylinder, it depends on the ratio of the diameter and the height, but when the diameter is about twice the height, *N* is to be 1/2. At this point, the demagnetizing factor (*N*) can be approximated as the average of the values of each of the finely divided parts of the magnet and the demagnetizing factors are calculated by micromagnetic simulation from modeling of the magnetic system and plotted in Figure 2.5. Using this term, *H*-field and *B*-field can be expressed below.

$$H = H_{app} + H_d \approx H_{app} - NM$$

$$B = \mu_0 \left(H + M \right) \approx \mu_0 \left(H_{app} - NM + M \right) = \mu_0 \left(H_{app} + \left(1 - N \right) M \right)$$

Each kinds of hysteresis curve have several characteristics. When the magnetic moment is saturated, the *B*-field is in a simple proportional relationship with a constant of μ_0 for *H*-field and the applied magnetic field. Figure 2.6 (a) shows the hysteresis curve assuming various demagnetizing factor (*N*) for the $M(H_{app})$ curve of a typical permanent magnet in Figure 2.4 (a). When a magnet is used in practice, most of the cases do not have an applied magnetic field, so the remanent magnetization M_r and the remanent magnetic flux density (remanent magnetic flux) B_r, which are the values when $H_{app} = 0$, are important values for estimating the performance of the magnetic material. do. As mentioned above, the demagnetizing factor *N* varies depending on the shape of the magnetic material and the relative magnetization direction, and as shown in Figure 2.6 (b), it has a completely different B_r value for the same $M(H_{app})$ curve, which has almost the same intrinsic properties. This is because $B_r = \mu_0 (1 - N) M_r$ is a strong permanent magnet having high squareness hysteresis loop, so even if the M_r value does not change by the shape, it can have the demagnetizing factor (*N*), that is, the remanent magnetic flux B_r value very different depending on the shape. The important point is that the $M(H_{app})$ curve can also vary depending on the shape of the magnetic body. There is little difference in the case of a very strong permanent magnet, but a different hysteresis curve is measured according to the shape of a general magnetic material. This is determined by the relative size between the shape anisotropy and the magnetocrystalline anisotropy. In the case of a strong permanent magnet having rare earth element such as NdFeB, almost the same $M(H_{app})$ curve is measured unless it is in the form of a very thin film because magnetic anisotropy is much larger than shape magnetic anisotropy. But in the case of soft magnetic materials, very different $M(H_{app})$ curve can be measured if the shape of the magnet changes due to shape magnetic anisotropy.

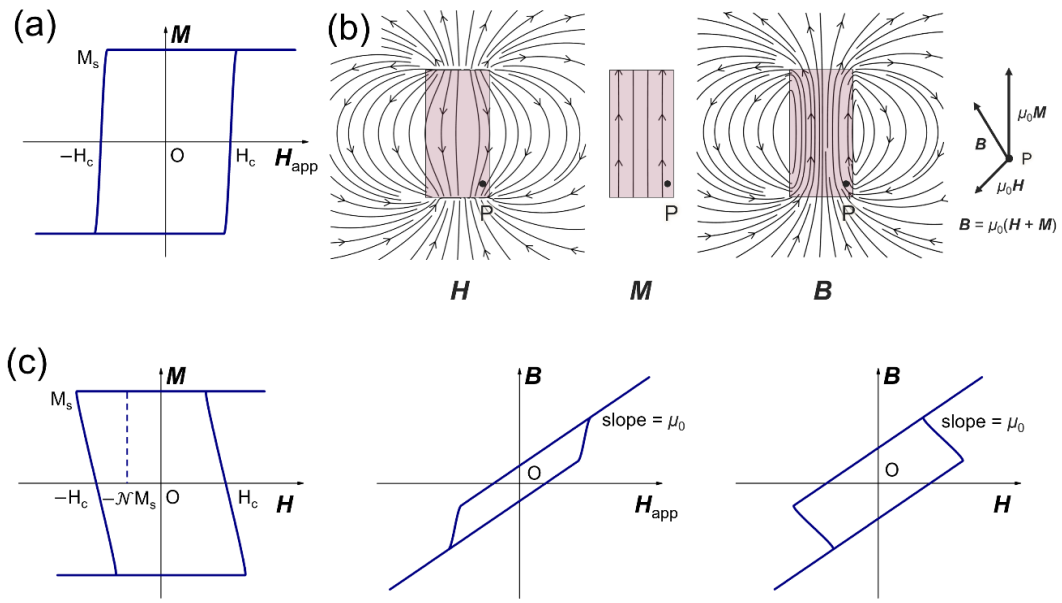

Figure 2.4 (a) Magnetization, M for a permanent magnet as a function of the applied field, H_{app}. (b) Distribution of the magnetic field strength, H, the magnetization, M, and the magnetic flux density, B, as well as their relation at the point P inside the magnet. (c) M, and B for a permanent magnet as a function of the applied field, H_{app} or the internal field, H. M_s, H_c, and N indicate the saturation magnetization, the coercivity, and the demagnetizing factor, respectively.

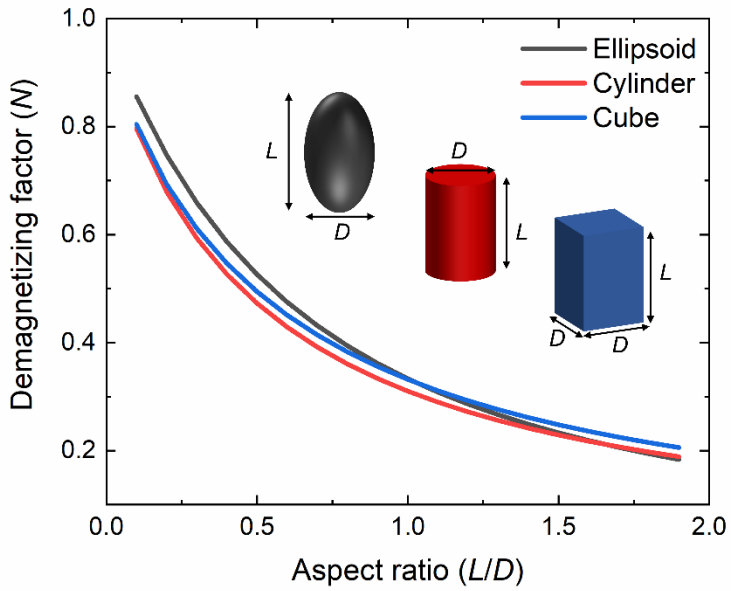

Figure 2.5 Demagnetizing factor (N) calculated by micromagnetic simulation. The change of demagnetizing (N) by aspect ratio change of ellipsoid, cylinder, cube structure having diameter (D), and height (L) is plotted.

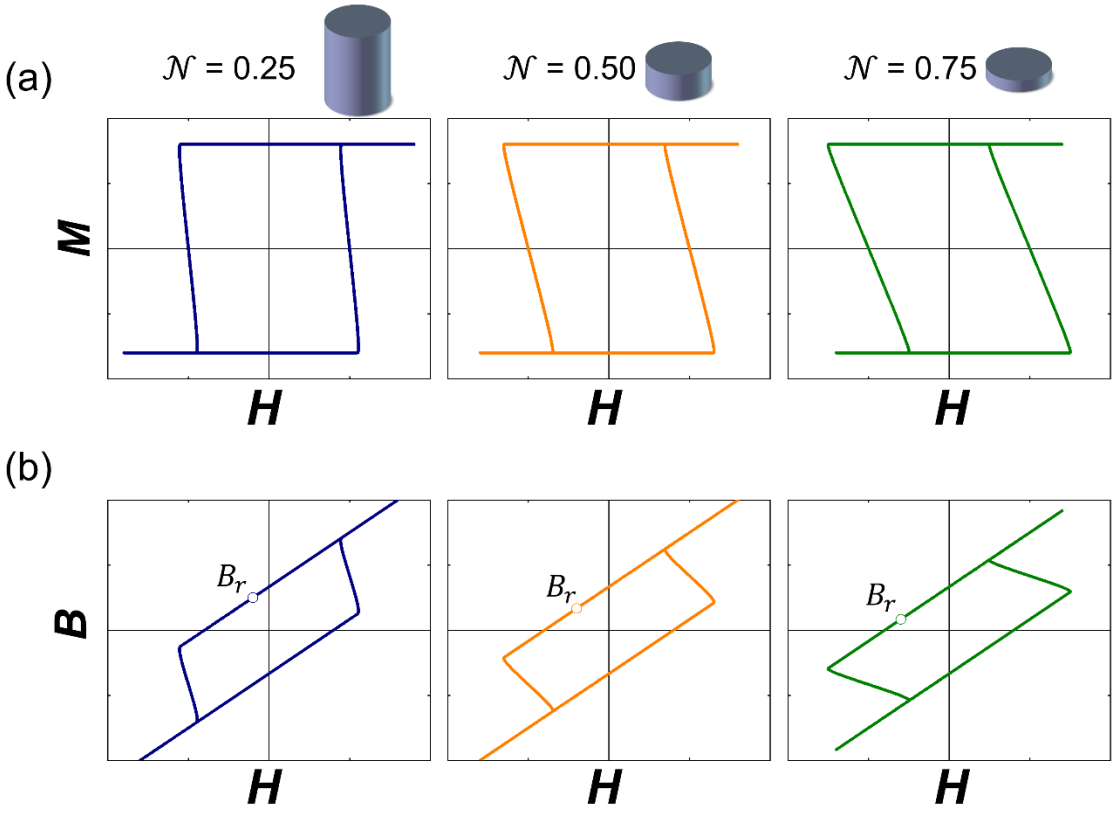

Figure 2.6 Hysteresis loops of the magnetization, M (a) and the magnetic flux density, B (b) as a function of the internal field, H with various demagnetizing factor N = 0.25, 0.5, and 0.75. B_r indicates the remanent magnetic flux density.

2.4 Energy Product

The Energy produced by a magnet can be largely divided into magnetostatic energy formed inside the magnet and outside the magnet [16]. In general, using a magnet means using the magnetic field around the magnet generated from it, so it is necessary to calculate the energy from the external magnetic field. First, the self-magnetostatic energy (E_m) formed inside a magnet with a volume of V is usually defined by the following equation.

$$E_m = -\frac{1}{2}\int_V \mu_0 H_d \cdot M \, d^3r$$

Since M is to be zero outside the magnet, it becomes the same value even if it is integrated over all spaces in from the equation. Since there is no applied field, $B = \mu_0 \left(H_d + M \right)$ and thus $M = B/\mu_0 - H_d$ and rewriting the above equation is as follows.

$$E_m = \frac{1}{2}\int_{\text{all space}} \left(\mu_0 H_d^2 - B \cdot H_d \right) d^3r$$

Applying the fact that $\int_{\text{all space}} B \cdot H_d \, d^3r = 0$,

$$E_m = \frac{1}{2}\int_{\text{all space}} \mu_0 H_d^2 \, d^3r$$

The energy produced by H-field can be obtained as $\frac{1}{2}\int_{V'} B \cdot H \, d^3r$ for given space (V) and $B = \mu_0 H$ in free space, so the energy is expressed below.

$$E = \frac{1}{2}\int_{V'} \mu_0 H^2 \, d^3r$$

Therefore, the energy from demagnetizing field (H_d) that the magnet we want to find out can be calculated as flows by applying upper equations to all spaces except for the magnet inside.

$$E_{out} = \frac{1}{2}\int_{all\ space-V} \mu_0 H_d^2 \, d^3r = \frac{1}{2}\int_{all\ space} \mu_0 H_d^2 \, d^3r - \frac{1}{2}\int_V \mu_0 H_d^2 \, d^3r$$

$$E_{out} = -\frac{1}{2}\int_V \mu_0 H_d \cdot M \, d^3r - \frac{1}{2}\int_V \mu_0 H_d^2 \, d^3r$$

Finally, the energy generated by the magnet to the outside follows next equation.

$$E_{out} = -\frac{1}{2}\int_V B \cdot H_d \, d^3r$$

That is, the energy outside the magnet can be obtained by integrating the inner product of the B-field inside the magnet and demagnetizing field (H_d). From this equation, the meaning of the energy product, which is used as figure-of-merit for estimating the performance of the magnet, can be seen. The energy

product expressed by the spatial integration formula $-\int_V B \cdot H_d \, d^3r$ inside the magnet is twice the energy outside the magnet from the magnetic field generated by the magnet. In particular, the important thing is that *H*-field inside the magnet for the energy product at remanent state is only the magnetizing field.

The energy of the magnetic field generated by a magnet to the outside is basically when there is no external magnetic field applied. If there is an external magnetic field, the energy is supplied form the outside, so only the energy of the magnet itself is not included. Therefore, only the remanent magnetic flux (B_r) and the remanent magnetization (M_r) are related to the energy produced by the magnetic materials in a given magnetic hysteresis curve. That is, the energy per unit volume can be expressed by the product of the remanent magnetic flux (B_r) and the demagnetizing field (H_d) created by the remanent magnetization (M_r).

$$-B \cdot H_d = -B_r \left(-NM_r\right) = -\mu_0 \left(-NM_r + M_r\right) = -\mu_0 \left(N^2 - N\right) M_r^2$$

The demagnetizing field is directly related to the value of the demagnetizing factor (*N*), which is determined by the shape of the magnet. This means that even with the same magnetic material, the energy product is different depending on the shape and direction of the magnetization. According to upper equation, it can be seen that there is little energy in the case where the demagnetizing factor *N* is made in the form of a thin film close to 1 or a needle-like shape where *N* is close to 0. In addition, the maximum energy product can be inferred from this equation. In general, in the case of a strong permanent magnet, it can be considered that the remanent magnetization (M_r) is almost the same as the saturation magnetization (M_s) regardless of the shape and the magnetization direction. In this case, the equation can be converted to next below equation.

$$-B \cdot H_d = \mu_0 \left(N^2 - N\right) M_s^2$$

And the energy is maximized with $\left(BH\right)_{\max} = \mu_0 M_s^2 / 4$ at $N = 1/2$. Normally, since the remanent magnetization is smaller than the saturation magnetization, it generally follows relationship.

$$\left(BH\right)_{\max} < \mu_0 M_s^2 / 4$$

In other words, the theoretical maximum energy product per unit volume is a value that depends only on the saturation magnetization (M_s), and the shape of the magnet is $N = 1/2$. Assuming a cylindrical magnetic material, as mentioned before, the diameter is about twice the height. However, in general since the remanent magnetization is not the same as the saturation magnetization and varies depending on the shape. In principle, in order to know the exact value of the maximum energy product for given magnetic material, the magnet should be manufactured in various shapes and the energy product should be calculated from the remanent magnetization according to each shape. However, since it takes a lot of time and effort to obtain the maximum energy product in this way, the maximum energy product is

usually obtained from the hysteresis curve of one shape through several assumptions. The energy product can be obtained from the $B(H)$ curve in Figure 2.6 (b). As previously discussed, the energy product is $-B_r\left(-NM_r\right)$, which is a point on second quadrant point making area of a rectangle created by a line perpendicular to the x and y axes when there is no external magnetic field ($H_{app} = 0$), and it is shown in Figure 2.7 (a). The straight line passing through the origin and the point in second quadrant is called a load line and has a different slope depending on the shape of the magnet (demagnetizing factor, N). In general, if the coercive force is sufficiently large and the remanent magnetization (M_r) does not vary according to the shape of the magnet, the $B(H)$ curve of the second quadrant becomes the same line regardless of the shape. In other words, when $H = 0$, B has a value of $\mu_0 M_r$, resulting in a straight line with a y-axis intercept of $\mu_0 M_r$ and a slope of μ_0. Thus, as shown in Figure 2.7 (b), if the $B(H)$ curves of the magnet with different shapes are drawn together in the second quadrant, the curves are drawn on the same straight line, and the magnets having different shape have different points $\left(-NM_r, B_r\right)$ called working points. If we obtain the resulting energy product, it can be expressed as in Figure 2.7 (c).

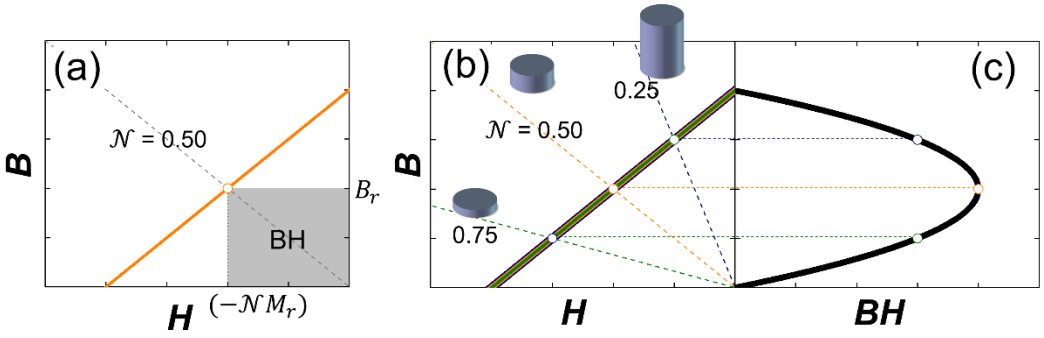

Figure 2.7 (a) The second quadrant of the *B*-*H* hysteresis loop with the demagnetizing factor $N = 0.5$. Shaded area indicates the energy product for given $N = 0.5$ at the remanent state. (b) The second quadrant of the *B*-*H* hysteresis loops for all three values of *N*. Open circles indicate the working point for given magnet shape (*N*) and the dotted lines crossing these points and the origin indicate the load lines.

2.5 Problem of Maximum Energy Product Prediction

In order to predict the maximum energy product of a magnet, in principle, the magnets having various shapes must be manufactured and the maximum value must be derived from the product of each remanent magnetic flux (B_r) and the demagnetizing field ($-NM_r$) at remanent state [16], [17]. As discussed in previous chapter, the second quadrant $B(H)$ curve is obtained for one shape, and the energy product according to the shape is inferred from the rectangular area created by a point of the curve and a line perpendicular to each axis, and the maximum energy product is predicted from this. In this chapter, the limitations of theses predicted value are covered.

First, I start by assuming the condition, where the magnetic hysteresis curve $M(H_{app})$ of the magnet does not change according to the shape of the magnet and the remanent magnetization (M_r) is the same as the saturation magnetization (M_s). In other words, the remanent magnetization and coercivity (H_c) are determined by the unique values of a given magnetic material. Here, the coercive force means H-field or an applied magnetic field (H_{app}) value at which the magnetization value or magnetic flux becomes 0 in the hysteresis curve. In the $M(H_{app})$ curve and the $B(H)$ curve, the coercivity has different values. In the $M(H_{app})$ curve the intrinsic coercivity (iH_c) and in the $B(H)$ curve the inductive coercivity (bH_c) are used, respectively.

If the $M(H_{app})$ curve is limited to not depend on the shape, iH_c, the intrinsic coercive force, does not change according to the shape of the magnet. However, since the $B(H)$ curve is highly dependent on the shape, the inductive coercive force bH_c also varies largely depending on the shape. In principle, the energy product has no relation with the coercive force since it is determined by the remanent magnetization (M_r) without the external magnetic field and the demagnetizing field at this time, but when predicting the maximum energy product from the magnet of one shape, an incorrect energy product may be derived due to his coercive force.

If the magnetic hysteresis loop does not depend on the shape of the magnet, it has the same remanent magnetization (M_r) in any shape and the remanent magnetic flux (B_r) is $\mu_0(1-N)M_r$, so a straight line that depends only on the demagnetizing factor as shown in Figure 2.7 (b). And this straight line passes through both the x and y axes. When the coercive force is large enough (usually when the intrinsic coercivity iH_c is larger than $\mu_0 M_s$), the $B(H)$ curve of the second quadrant becomes the same line regardless of the shape and the x-axis intercept of the y-axis is the same. By measuring only magnet of an arbitrary shape, energy product of all shapes can be derived without problems. An shown in Figure 2.8, there is no problem in deriving the maximum energy product form the $\mu_0(H_{app}+M)$ curve along H_{app}, which is a method that is mainly used experimentally, because it is also represented by the same straight line in the second quadrant.

Figure 2.9 shows the $M(H_{app})$ curve $B(H)$ curve of the second quadrant according to the various coercive forces and the demagnetizing factor (N), the $\mu_0\left(H_{app}+M\right)$ curve according to H_{app}, and the energy product predicted from each curve. If the coercive force is less than the saturation magnetization (M_s), the hysteresis curves of the second quadrant do not appear as a single straight line but become a broken line and the predicted value of the energy product is different from the original value. In the case of the load line with a low demagnetizing factor, the energy product is predicted well, but wrong value of the energy product is predicted above a certain demagnetizing factor. Since the purpose of predicting the energy product is to know the maximum energy product of a given magnetic material, it is only necessary to correctly deduce the maximum energy product even if an incorrect prediction is made above a certain value. However, as shown in Figure 2.9, depending on the coercive force, the maximum energy product can be incorrectly predicted.

Firstly, let us focus on the case of predicting the maximum energy product with $\mu_0\left(H_{app}+M\right)$ curve along H_{app} (the curve shown in navy line in Figure 2.9). The curve has no relation to the demagnetizing factor because it does not include any parameters depending on the shape of the magnet. When the demagnetizing coefficient is $N = 1/2$, the maximum energy product is obtained. Therefore, in order to correctly predict the maximum value, the energy product must be correctly predicted up to the demagnetizing factor corresponding to this value. So, the intrinsic coercivity iH_c should be at least larger than $1/2M_s$. On the other hand, since the $B(H)$ curve is affected by the shape of the magnet, that is, since the demagnetizing factor, if the coercive force is small, the slope of the load line (demagnetizing factor, N) from which erroneous energy product prediction starts is determined depending on the shape. Finally, in some case of the shape, the maximum energy product is incorrectly predicted. However, when the intrinsic coercivity iH_c is greater than $1/2M_s$, the maximum energy product of any shape can be correctly predicted, and even when the intrinsic coercivity is less than $1/2M_s$, the prediction for the maximum energy product is always correct for a shape having a demagnetizing factor larger than 1/2.

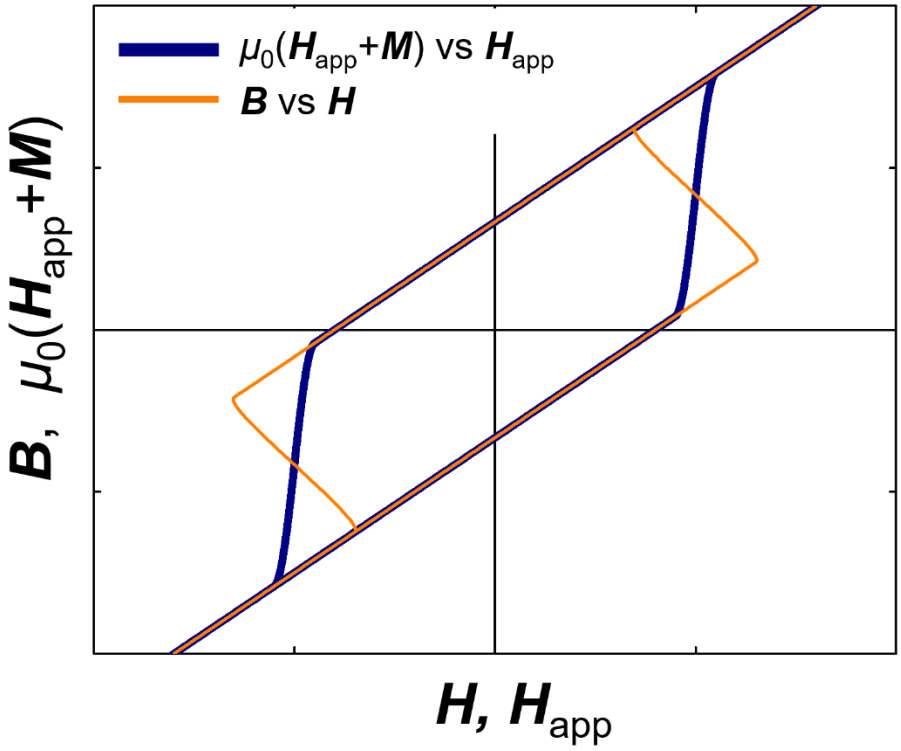

Figure 2.8 The hysteresis loop of $\mu_0\left(\boldsymbol{H}_{app}+\boldsymbol{M}\right)$ as a function of the applied field, $\boldsymbol{H}_{app}$ and the magnetic flux density, $\boldsymbol{B}$ as a function of the internal field, $\boldsymbol{H}$.

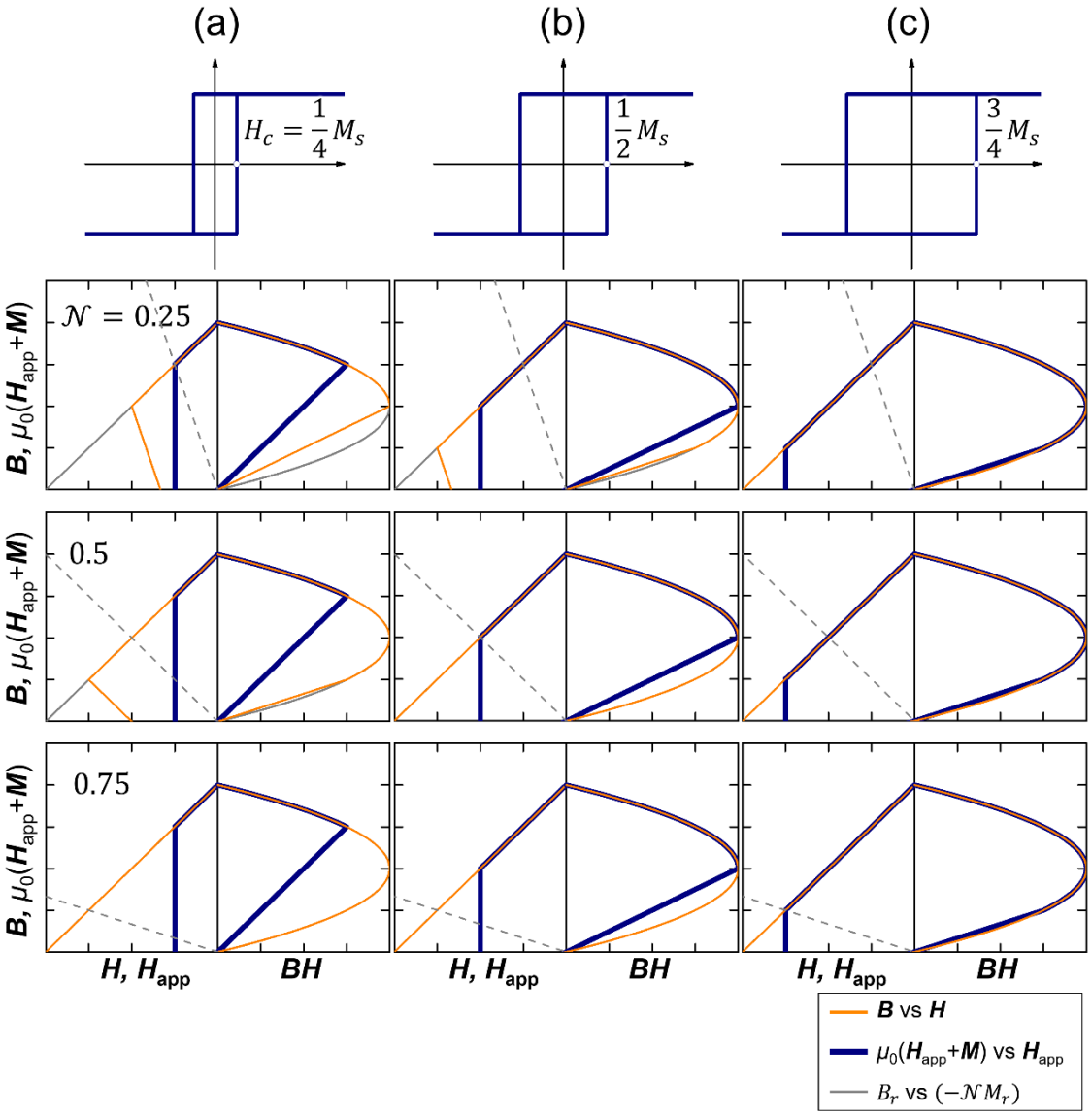

Figure 2.9 The second quadrant of the *B*-*H* and $\mu_0\left(\boldsymbol{H}_{\text{app}}+\boldsymbol{M}\right)$ - $\boldsymbol{H}_{\text{app}}$ hysteresis loops and the estimation of the energy product (*BH*) from them with different shape (different values of the demagnetizing factor, N) for three permanent magnets with different coercivities of $H_{\text{c}}/M_{\text{s}}=1/4$ (A), $1/2$ (b), $3/4$ (c). The gray line in each *BH* panel indicates the true energy product (*BH*) since it obtained from the remanent magnetic flux density, B_{r} and the internal field $\boldsymbol{H}=-NM_{\text{r}}$ for all values of N (see the gray lines in the *B*-*H* loop panel).

In the case of a general magnetic material, if the remanent magnetization is not the same as the saturation magnetization according to various extrinsic factors such as microstructure, and the magnetic anisotropy inherent in the magnetic material is not sufficiently large, the hysteresis curve $M(H_{app})$ is sensitively changed according to the shape of the magnet. Figure 2.10 shows how differently the energy product can be predicted according to the shape when the remanent magnetization (M_r) is not the same as the saturation magnetization M_s even though the hysteresis curve $M(H_{app})$ does not change according to the shape of the magnet. Both the $\mu_0\left(H_{app}+M\right)$ curve and the $B(H)$ curve according to H_{app} show a lot of difference from the slope of the straight-line graph that appears according to the shape of the remanent magnetic flux (B_r) and the remanent demagnetizing field in the second quadrant. Accordingly, there may be a significant difference from the energy product predicted by the hysteresis loop and the actual remanent magnetic flux (B_r) and the remanent demagnetizing field. As shown in the graph on the right of Figure 2.10, the $\mu_0\left(H_{app}+M\right)$ curve according to H_{app} predicts incorrect values in all sections except 0, and the $B(H)$ curve also predicts incorrect values other than the values for the given shape. If the hysteresis curve $M(H_{app})$ is sensitively changed to the shape of the magnet, since the remanent magnetic flux and the remanent demagnetizing field at this time lose a linear proportional relationship according to the shape, the prediction by the hysteresis curve is impossible. Moreover, the maximum energy product value may have a maximum value at a value other than the demagnetizing factor of $N = 1/2$. Therefore, in this case, it is necessary to derive the maximum energy product by making various shapes of the magnetic material.

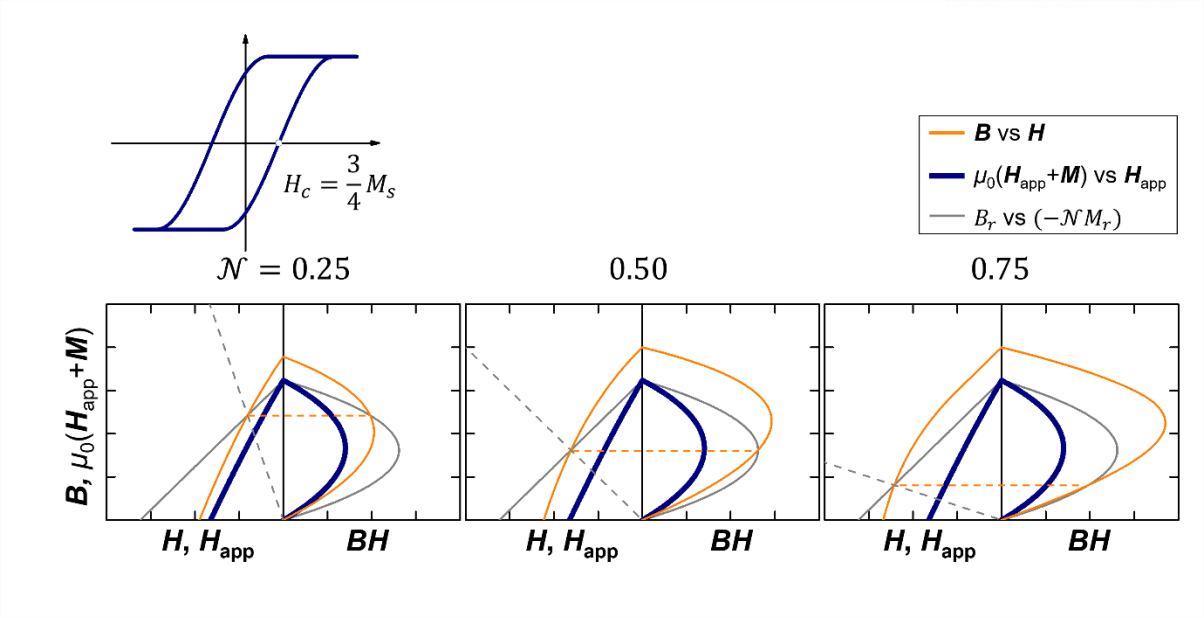

Figure 2.10 The second quadrant of the *B*-*H* and $\mu_0\left(\boldsymbol{H}_{\text{app}}+\boldsymbol{M}\right)$-$\boldsymbol{H}_{\text{app}}$ hysteresis loops and the estimation of the energy product (*BH*) from them with different shape (different values of the demagnetizing factor, N) for the permanent magnets with the remanent magnetization, M_{r} which is different from the saturation magnetization, M_{s}.

3. Research Methods

3.1 Micromagnetic Simulation

The micromagnetic simulation is the numerical tool to solve the micromagnetic problem, such as the magnetization switching, and dynamics of the magnetic structure, in the nano- and micro-scaled magnetic medium. Comparing with first principle method calculating fully quantum mechanical wave function for the atomic nature of materials, the micromagnetic simulation is based on micromagnetics which is basic theory to use classical physics with the continuum approximation. The main task of the micromagnetic simulation is tracking energetically equivalent magnetization configuration considering micromagnetic energies through the minimization of the total free energy using variational calculus. There are a variety of micromagnetic energies. Although there are many kinds of the micromagnetic energies, the representative energy terms for permanent magnet are considered such as exchange energy, demagnetization energy, magnetocrystalline anisotropy energy, and Zeeman energy. Detailed energy terms considered in the micromagnetic simulation is introduced in Ch.2.1.

The first thing to solve the magnetic problem by using micromagnetic simulation is to establish the discretized magnetic geometry. The discretized geometry is composed of micromagnetic cells, and the magnetization having the material information is assigned to each cell. In general, the size of the micromagnetic cell should be selected below the exchange length, which is the length scale where the magnetization changes smoothly without strong inhomogeneity. In the micromagnetic simulation, finite different method (FDM) and finite element method (FEM) are widely used to discretize the geometry. There are a variety of micromagnetic simulation codes. In this thesis, mumax3 code developed by Ghent University is adopted for the simulation [10], which has an advantage in fast computing speed by using graphical processing unit (GPU) acceleration and uses finite different method (FDM).

There are several advantages on using the micromagnetic simulation for studying permanent magnet. The one thing is that the study via simulation can convert the resource for investigation. For instance, the cost for the simulation is determined by the calculation size, not by the price of the material or the experimental equipment. Thus, various materials and condition can be calculated according to physical properties. The strongest factor of the micromagnetic simulation is that the physical quantities of all positions can be known individually. From the physical quantities, we can assemble or calculate what we want to know about the system. Especially, it is hard to visualize or measure the magnetic field from the magnetic materials. To overcome the limitation of measurement for the magnet, I have carried out various micromagnetic simulation for enhancing the energy product of magnets.

4. Effect of Microstructure on Magnetic Properties

4.1 Anisotropy Distribution

Before modeling microstructure for a magnet, how microstructure of the magnet is composed should be understood. As discussed in previous chapter, magnetic material for the permanent magnet has high crystalline anisotropy energy along its easy axis affected by the crystal structure. In general, a magnet is composed of many grains, each grain has its own crystal orientation with certain distribution, which has largely affected the performance of the magnet including the coercivity and the energy product [9], [18]–[28]. From Stoner-Wohlfarth model assuming a certain deviated angle from the easy axis, the remanent magnetization (M_r), which is an important element for determining the energy product at the remanent state, is decreased by increasing the deviated angle from the easy axis of the magnet.

$$BH = -B \cdot H_d = -\mu_0 \left(N^2 - N \right) M_r^2$$

Thus, magnet consists of grains perfectly aligned along the easy axis has theoretically highest energy product. However, it is difficult to make perfectly aligned magnets unless they are made of a single crystal. Moreover, Kronmüller et al. showed that the coercivity of a magnet should be determined by the minimum nucleation field for misaligned grain and the degree of grain alignment results in weak angular dependence of the coercivity due to the effects of the reversal of the misaligned grains emitting local stray field [23], [29]–[31]. To reduce the loss of the energy product because of the misalignment, when synthesizing the magnet, it goes through the process of aligning the direction of the crystal in the grain structures inside the magnet with strong external magnetic force [32]–[34]. From this process, the anisotropy of the grains in the magnet follows a certain distribution. To obtain high energy product and designing the microstructure of a magnet, understating the crystal anisotropy alignment of the general magnet should be studied. Much research about the degree of the alignment have already been carried out. As a result, the direction of the crystal structure in the magnet with the magnetic field applied during the synthesis follows normal Gaussian distribution as presented below [35].

$$P(\theta) = \frac{1}{\sqrt{2\pi}\sigma} \exp\left(-\frac{\theta^2}{2\sigma^2} \right)$$

Where θ is the deviated angle from the easy axis, and σ is the orientation distribution coefficient representing the degree of grain easy-axis alignment. This function can be simplified by changing θ to $\tan\theta$ because the sign of the deviated angle is meaningless according to the magnetic energy. So, the distribution can be described by following function and expressed in Figure 4.1.

$$P(\theta) = \frac{1}{\sigma}\sqrt{\frac{2}{\pi}} \exp\left(-\frac{\tan^2\theta}{2\sigma^2} \right)$$

Where $0 \le |\theta| \le \pi / 2$.

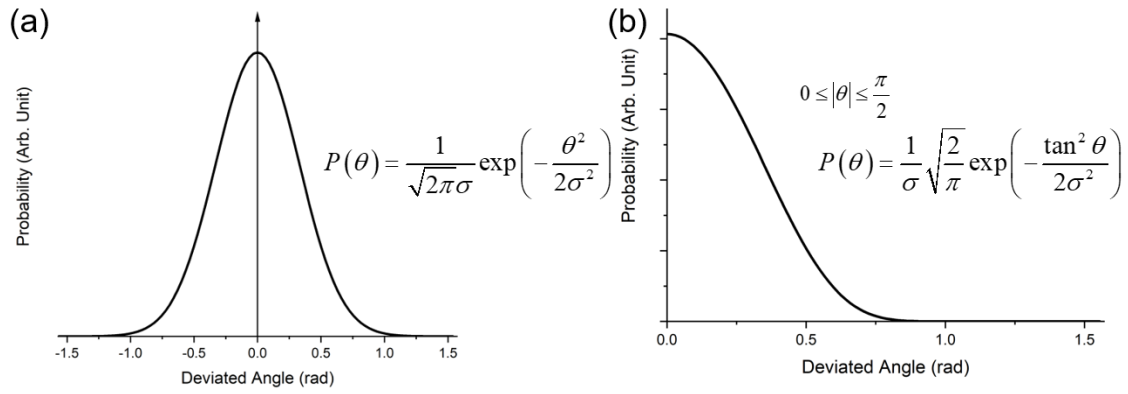

Figure 4.1 (a) Normal Gaussian distribution for the deviated angle from the easy axis of the magnet having the uniaxial crystalline anisotropy. (b) "tan-type" Gaussian distribution.

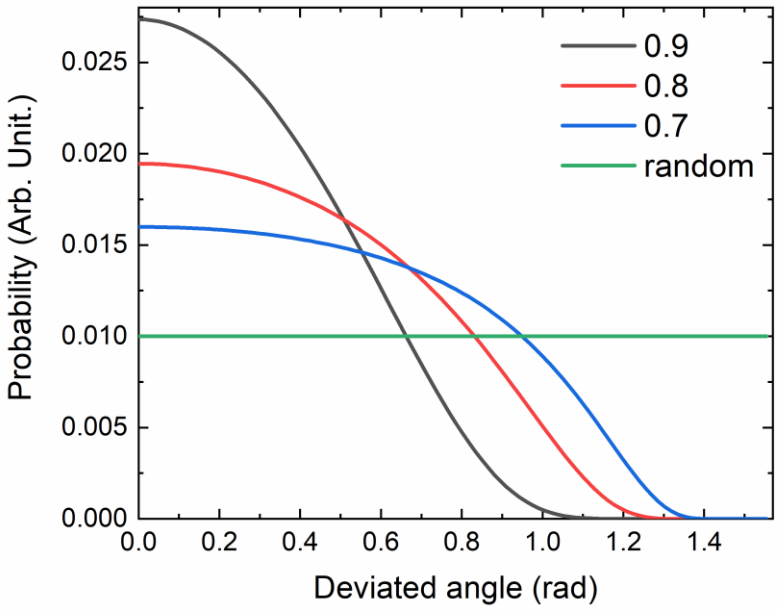

Figure 4.2 Probability by the deviated angle from the easy axis for different alignment α.

The degree of the alignment can be expressed by following equation.

$$\frac{M_r}{M_s} = \int_0^{\frac{\pi}{2}} P(\theta)\cos\theta \, \mathrm{d}(\tan\theta)$$
$$= \frac{1}{\sigma}\sqrt{\frac{2}{\pi}}\int_0^{\infty} \exp\left(-\frac{x^2}{2\sigma^2}\right)\frac{\mathrm{d}x}{\sqrt{1+x^2}} = \cos\bar{\theta} = \alpha$$

Where the ratio of the remanent magnetization (M_r) to saturation magnetization (M_s) or by the average deviated angle from the easy axis represent the degree of the alignment (α). For instance, the probability function by the deviated angle with different standard deviation is calculated and plotted in Figure 4.2. From this equation, the function of the degree of alignment to the change of the orientation distribution coefficient representing the degree of grain along easy axis alignment (σ) is calculated and expressed as shown in Figure 4.3, and the distribution of grain alignment is used in all the study about the microstructure after this chapter.

In order to elucidate the relation between the degree of anisotropy alignment and magnetic hysteresis curve, the simple magnetic structure composed of $Sm(FeCo)_{12}$ by micromagnetic simulations according to various standard deviation value for tan-type Gaussian distribution. As a model system, I adopt the 200 × 200 × 200 nm^3 sized cube in which the microstructure is formed in grains having different anisotropy direction as shown in Figure 4.4. I assumed that the easy axis of magnetocrystalline anisotropy is z-axis and it distributes normally in each grain with standard deviation of 0.55, 0.95, and 1.44. The hysteresis loops were calculated by applying external magnetic field ranging from -10 T to 10 T along z-axis. As shown in Figure 4.5, the remanent magnetization (M_r) varies dramatically according to the alignment (α) and resulting coercivity and the energy product is represented in Table 4.2. From the simulation results, the remanent magnetization is almost corresponding with the expectation value from the equation. Because the remanent magnetization is decreased in low anisotropy alignment structure, the energy product is directly affected by the change the remanent magnetization. Even if the grains in the magnet is not perfectly aligned along the easy axis, the value of energy product is almost six times larger than that of the randomly aligned structure. Thus, aligning anisotropy direction of the grains inside the magnet by the external magnetic field affects largely the performance of the magnet.

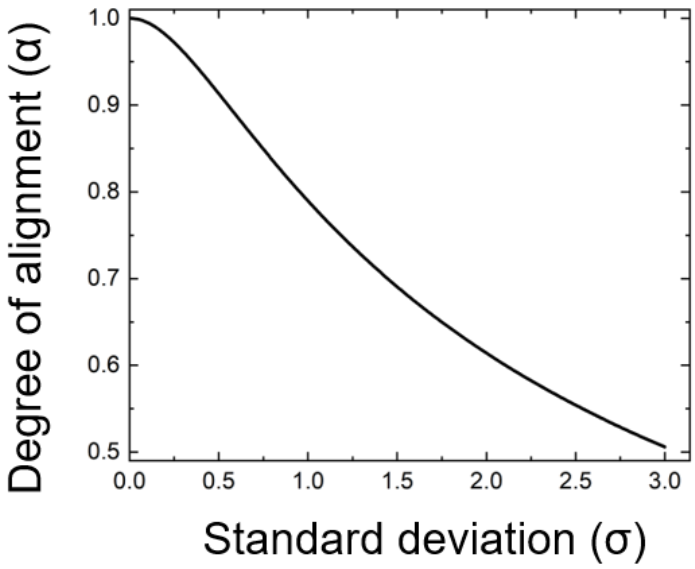

Figure 4.3 Degree of the alignment as a function of the orientation distribution coefficient representing the degree of grain easy-axis alignment.

Alignment (α)	**Std. (σ)**	**Average angle ($\bar{\theta}$)**
0.9	0.55	25.84
0.8	0.95	36.87
0.7	1.44	45.57

Table 4.1 Calculated degree of the alignment (α) and average angle ($\bar{\theta}$).

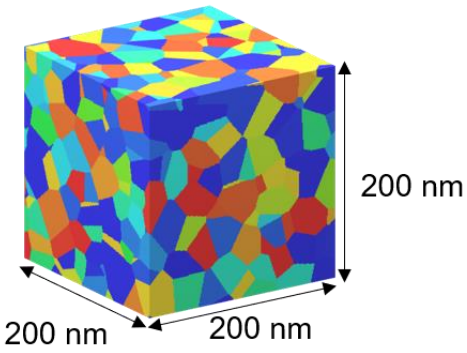

Figure 4.4 Model system of $Sm(FeCo)_{12}$ magnet composed of 30 nm size grains with various easy axes.

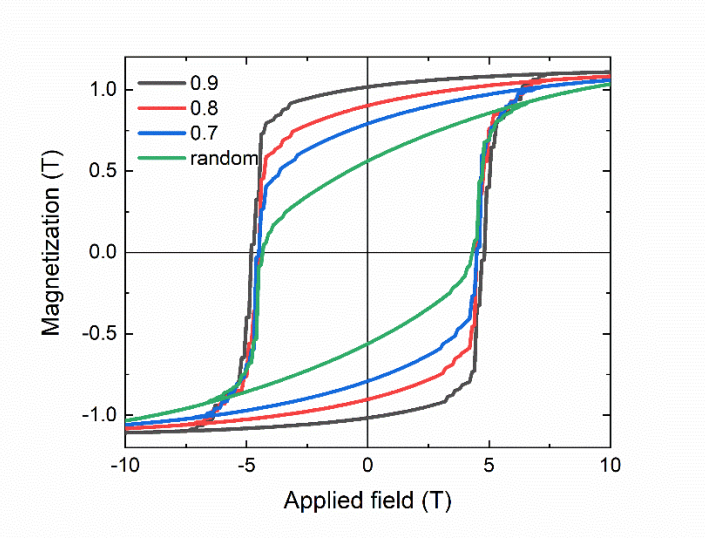

Figure 4.5 Calculated magnetic hysteresis curve $M(H_{app})$ for various degree of the alignment (α).

Alignment (α)	Coercivity (T)	Remanence (M_r/M_s)	BH (MGOe)
0.9	4.81	0.89	23.21
0.8	4.48	0.79	17.43
0.7	4.49	0.69	12.41
random	4.34	0.49	4.64

Table 4.2 Simulation results including the coercivity and the ratio of remanent magnetization, and the energy product.

4.2 System shape

As mentioned in previous chapter, the shape of a magnet affects the demagnetizing factor, which results in the change of the slope of the load line. So, the energy product is changed by the shape of the magnet. The hysteresis curves showing the $M(H_{app})$, $M(H)$, $B(H_{app})$, and $B(H)$ are investigated by the micromagnetic modeling, which is assumed composed of a single grain structure. The magnetic material for the model is MnBi, which have high anisotropy energy, but relatively low saturation magnetization of 0.63 T for the anisotropy field. As a model system, tetragonal structure having various aspect ratio of diameter to height of the magnet is used to study the effect of the system shape, and the schematic image, $B(H)$, and $B(BH)$ are shown in Figure 4.6. The hysteresis loops were calculated by applying external magnetic field ranging from -5 T to 5 T along z-axis, which is the easy axis of the system, and the hysteresis curves from the calculation are plotted on Figure 4.6.

From the simulation results, there is little difference in the coercivity between the microstructures having various aspect ratio, but the difference does not affect the energy product due to its high coercivity. In the case all the shape of the single grain magnet, the second quadrant of the $B(H)$ hysteresis curves is on the same line, which means that the only factor to determine the working point of the magnetic system is the demagnetizing factor (N) from the shape of the magnet because the coercivity does not have influence on the energy product if the value of the coercivity is enough high. In conclusion, the energy product can be controlled by the shape of the magnet in a single grain model having high enough crystalline energy, although the coercivity of each magnet is slightly different.

However, normal bulk magnet is not a single grained structure. To compare more realistic system, I set the model system having grain structure with the size of 20 nm, which is aligned with the degree of the anisotropy alignment with 0.9, and the schematic images and hysteresis loops are represented in Figure 4.8. Except for the multi-grain structure in the magnet, other condition is same with the single grain model shown previously. Even if the coercivity is high enough for the magnet, if the grain structure is considered, $B(H)$ curves does not lie on the same line, which means that the prediction for the energy product by manufacturing a magnet is more difficult as the microstructure gets more complex.

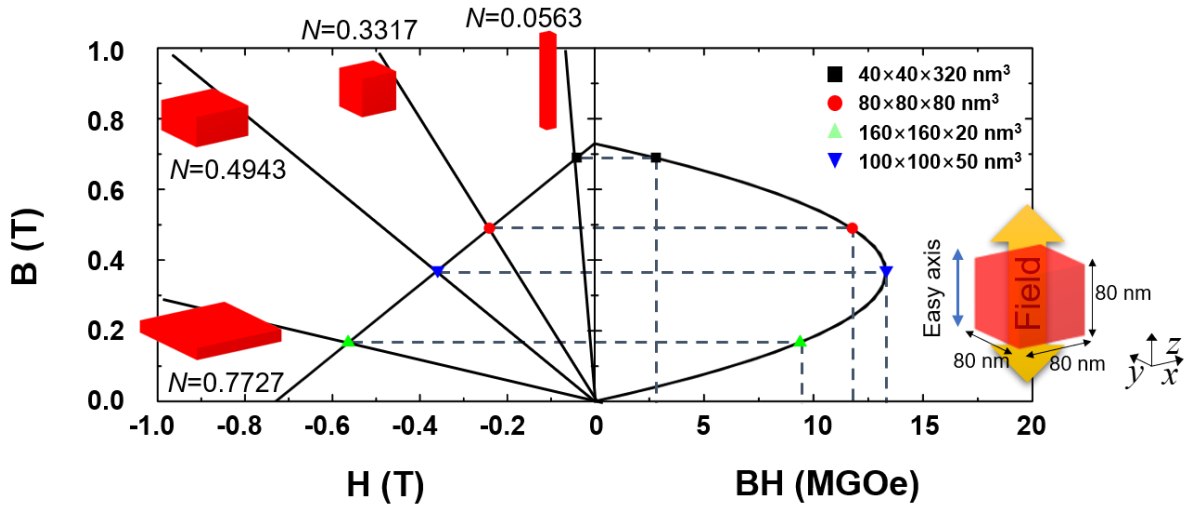

Figure 4.6 The hysteresis curves $B(H)$ and the energy product curve $B(BH)$ for various shapes of the single grain magnet having different aspect ratio and same volume.

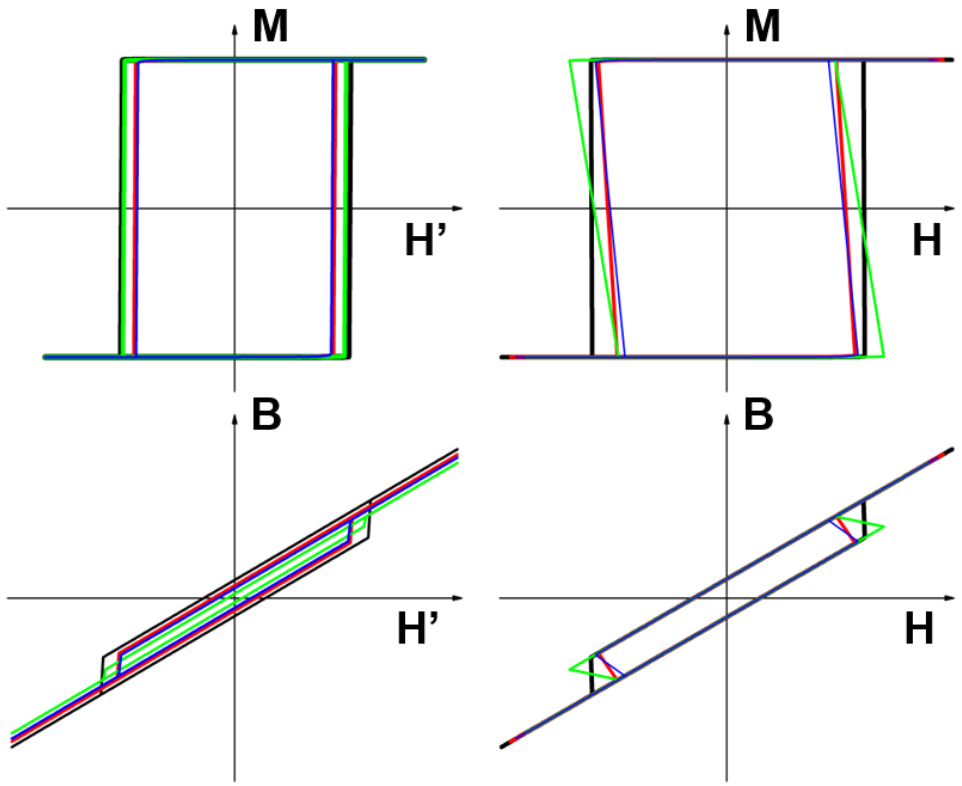

Figure 4.7 Four types of the hysteresis curves for model system shown in Figure 4.6.

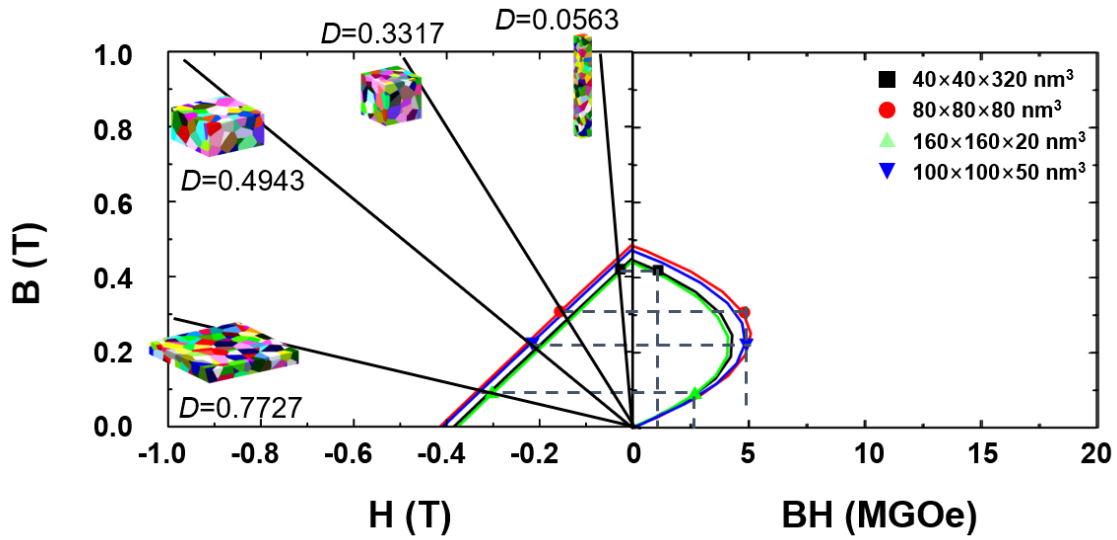

Figure 4.8 The hysteresis curves $B(H)$ and the energy product curve $B(BH)$ for various shapes of the multi-grain magnet having different aspect ratio.

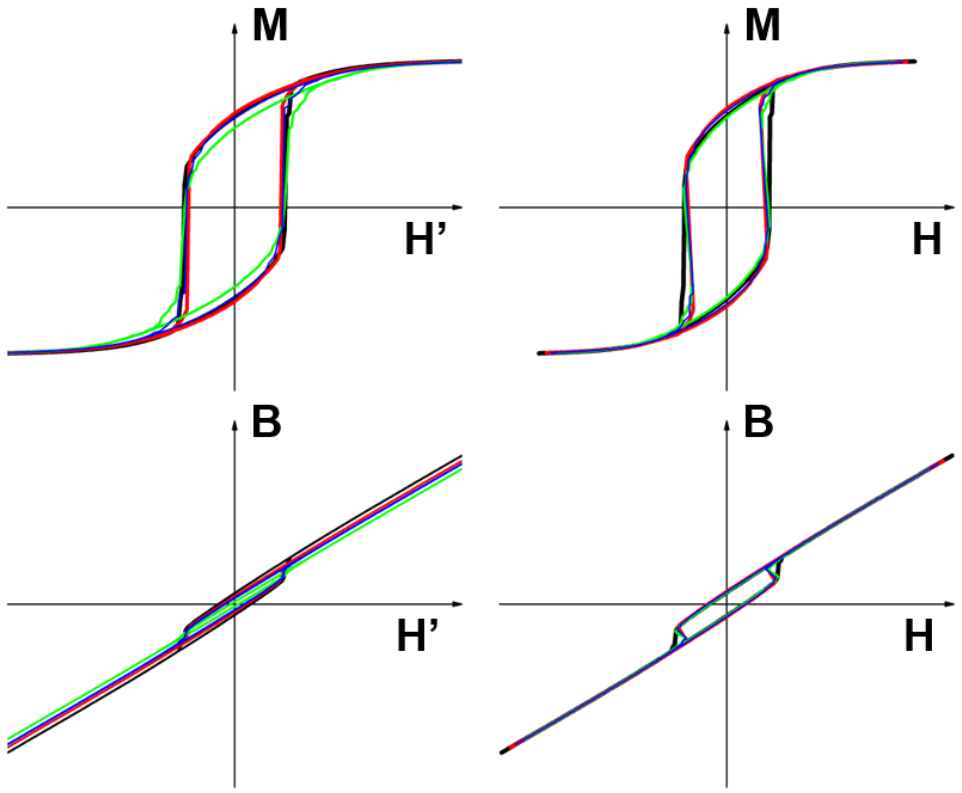

Figure 4.9 Four types of the hysteresis curves for the magnet having the aligned multi-grain nanostructures.

4.3 Grain Structure

4.3.1 Model System and Simulation Methods

The coercivity, as an extrinsic magnetic property, does not have direct relationship with the energy product of the magnet. However, as discussed in previous chapter, the poor coercivity results in limiting to have high energy product. Thus, coercivity should be controlled by microstructure of the magnet such as grain size, grain shape, grain boundary for approaching to the anisotropy field, which is intrinsic property. In order to understand the reason of resulting coercivity and improve the energy product by designing optimal microstructure, various characteristics of the microstructure must be studied [36]–[39].

In this chapter, the simulations via the micromagnetic solver have been carried out for investigating the magnetic properties of model systems having various microstructures. $Sm(Fe_{11}Ti_1)$ is selected as the material for the model system, which is one of the prominent candidates due to its high anisotropy field [47]–[50]. The anisotropy field, $H_A = 2K_1 / \mu_0 M_s$ is directly related to the crystalline anisotropy of the material, which means the potential coercivity of the magnet. I assumed that the z-axis was the easy axis of magnetization of the model system with a uniaxial crystalline anisotropy constant of 4.8 MJ/m^3 and it is distributed according to tan-type Gaussian distribution in each grain with standard deviation of 0.95, where the degree of the anisotropy alignment with 0.8. The exchange stiffness A_{ex} of 7.78×10^{-12} J/m and the saturation magnetization M_s of 907.18 kA/m^3 were assumed. In the finite differential calculation of the micromagnetic properties, a cubic cell of $1 \times 1 \times 1$ nm^3 was chosen, which was smaller than the exchange length of the material (1.27 nm). The exchange length is calculated by following equation.

$$l_{ex,M_s} = \sqrt{\frac{2A}{\mu_0 M_s^2}}, \quad l_{ex,K_1} = \sqrt{\frac{A}{K_1}}$$

Where A is the exchange stiffness and K_1 is uniaxial crystalline anisotropy constant. The exchange length is smaller value between two kinds of the exchange length, which are calculated from the saturation magnetization and the anisotropy constant. For the model microstructure, $200 \times 200 \times 100$ nm^3 sized cuboid in which the microstructure is composed of many grains having different average size of 30, 50, 100 nm, and schematic image of the microstructure is shown in Figure 4.10. The shape of the system is selected for maximizing the energy product and the grain size is considered as smaller size than the single domain size (400 nm) to focus on the effect by the pinning of domain propagation at the interface between grains.

Unlike the exchange interaction within a grain, the exchange coupling is diminished at the interface by several reasons such as the difference of the direction of the crystal structure, secondary phases created at the interface, the defects, and so on [10], [51]–[53]. Thus, the intergrain exchange interaction

is defined using the exchange stiffness A_{ex}, the saturation magnetization M_s, and intergrain exchange coefficient s, and it is expressed by following equation.

$$\vec{B}_{exc} = 2S \frac{2\dfrac{A_{ex1}}{M_{s1}}\dfrac{A_{ex2}}{M_{s2}}}{\dfrac{A_{ex1}}{M_{s1}} + \dfrac{A_{ex2}}{M_{s2}}} \sum_i \frac{(\vec{m}_i - \vec{m})}{\Delta_i^2}$$

Where s is an arbitrary scaling factor which may be used to alter the exchange coupling between grains, and s = 0.1 and 0.9 are considered for the simulation. To obtain full hysteresis loops, an external magnetic field ranging from −10 to +10 T was applied along the easy axis. To obtain the correct *BH* values, we calculated mean value of the dot product of *H* and *B* in each cell.

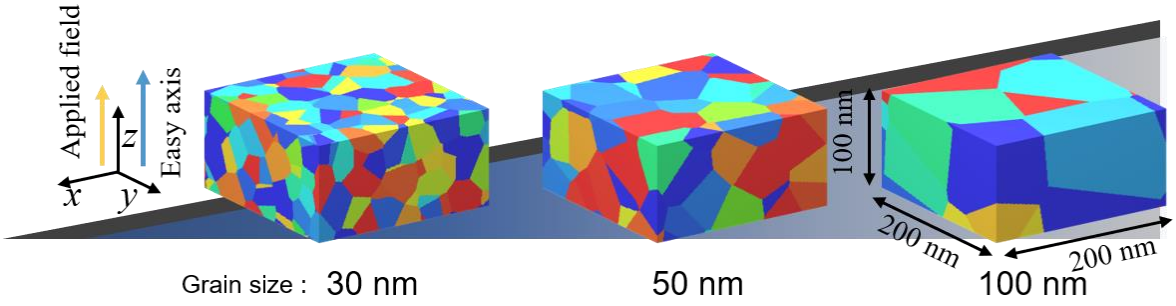

Figure 4.10 Schematic images of the modeled magnets with different value of average grain size. The structure is the size of 200 × 200 × 200 nm^3 and the external magnetic field is applied along the easy axis (z-axis).

Structure type	**Tc (K)**	**$\mu_0 H_A$ (T)**	**K1 (MJ/m^3)**
$ThMn_{12}$	584	10.5	4.8
$\mu_0 M_s$	**$(BH)_{max}$ (MGOe)**	**δ_ω (nm)**	**d_c (μm)**
1.14	32.5	4.0	0.4

Table 4.3 The structure type, intrinsic magnetic properties including the Curie temperature T_C, the anisotropy field H_A, the anisotropy constant K_1, the saturation magnetization, the theoretical limit of the energy product), the domain wall width and the critical single domain particle size of $Sm(Fe_{11}T_1)$ [24].

4.3.2 Simulation Results

At first, the simulated hysteresis curves $M(H_{app})$ of these models are shown in Figure 4.11. Largest difference between the model having difference intergrain exchange interaction (s) is the coercivity. The hysteresis curves with various average size of the grains with integrain interaction of 0.1 are simulated and plotted in Figure 4.11 (a). The hysteresis curves have similar tendency during reversal process, and the coercivity of the magnets are not that different. Because each grain is separated by the interface, the switching process also occurs, respectively following the anisotropy direction of each grain. When the magnetization of a grain is tilted by Stoner-Wohlfarth model having large deviated angle from the easy axis, the grain does not have large effect on neighboring grains, which causes delayed reversal of total system. Thus, the coercivity of weakly coupled microstructure is much larger than that of strongly coupled microstructure. However, in the case of the degree of the anisotropy alignment is 0.8, many of grains still does not switched at the remanent state, which results in enough high energy product even though the coercivity is decreased by almost half.

The value of the energy product is plotted in Figure 4.12. By the reduction of the remanent magnetization, the energy product is also decreased by the increase of the average grain size. There are reasons why the microstructure having smaller grain has higher coercivity. The first reason comes from the change of the nucleation mode. In the nucleation process, whether the magnetization inside the magnet is switched coherently or with creating curl has a great influence on the coercivity. However, the critical size changing the nucleation mode is almost 400 nm, and the model system is designed as the microstructure composed of grains under 100 nm to avoid the effect from the nucleation mode change. Thus, the increase of the coercivity in small sized grains has another reason, which is the increase of the interface area between neighboring grains. The area of interfacial region in a certain size of the magnet is inversely proportional to the average size of the grains. The increased area of the interfacial region decelerates the diffusion of the switched grains.

In order to analyze the reversal process, the schematic images of the switching magnet and the hysteresis curves to show the state are represented in Figure 4.13. The red colored grains are switching to the blue color by the external magnetic field applied along the opposite direction. While the Figure 4.13 (b) shows that the grains are switched respectively, most of the grains in Figure 4.13 (c) are switched right after the color of the small section of the grain is changed to blue. Figure 4.14 shows the direct comparison of models having different intergrain exchange interaction.

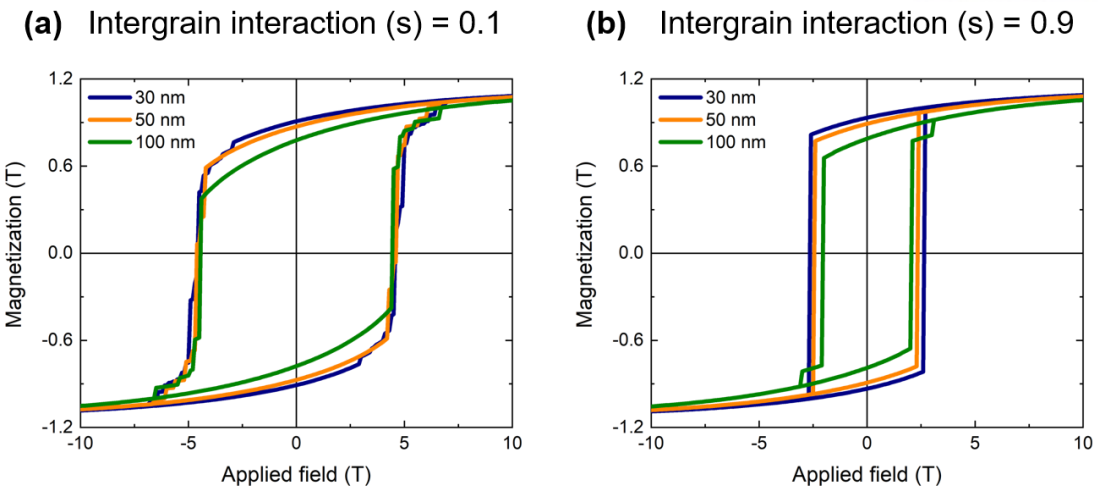

Figure 4.11 Magnetization curves of the simulated magnet for different average grain sizes of 30, 50, 100 nm. Intergrain exchange interaction (*s*) is considered as (a) 0.1, and (b) 0.9.

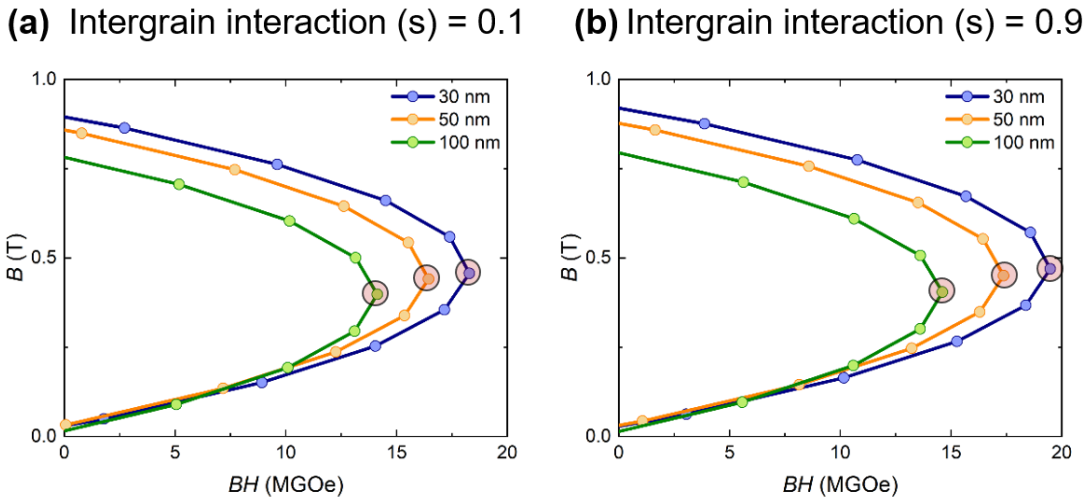

Figure 4.12 Energy product of the simulated system. Each circle on the graph means the value of calculated energy product at a certain external magnetic field, especially the points at the remanent state are in bigger red transparent circle. Intergrain exchange interaction (*s*) is considered as (a) 0.1, and (b) 0.9.

Intergrain exchange, *s*	**Grain size (nm)**	**Coercivity, H_c (T)**	**Remanent magnetization ,M_r (T)**	**Energy product, *BH* (MGOe)**
0.1	30	4.5739	0.9086	18.2851
	50	4.6084	0.8723	16.4475
	100	4.4392	0.7777	14.1318
0.9	30	2.6448	0.9331	19.4854
	50	2.4443	0.8914	17.3779
	100	2.0458	0.7891	14.6148

Table 4.4 The coercivity H_c, the remanent magnetization M_r, and the energy product values from the micromagnetic simulation of the model system.

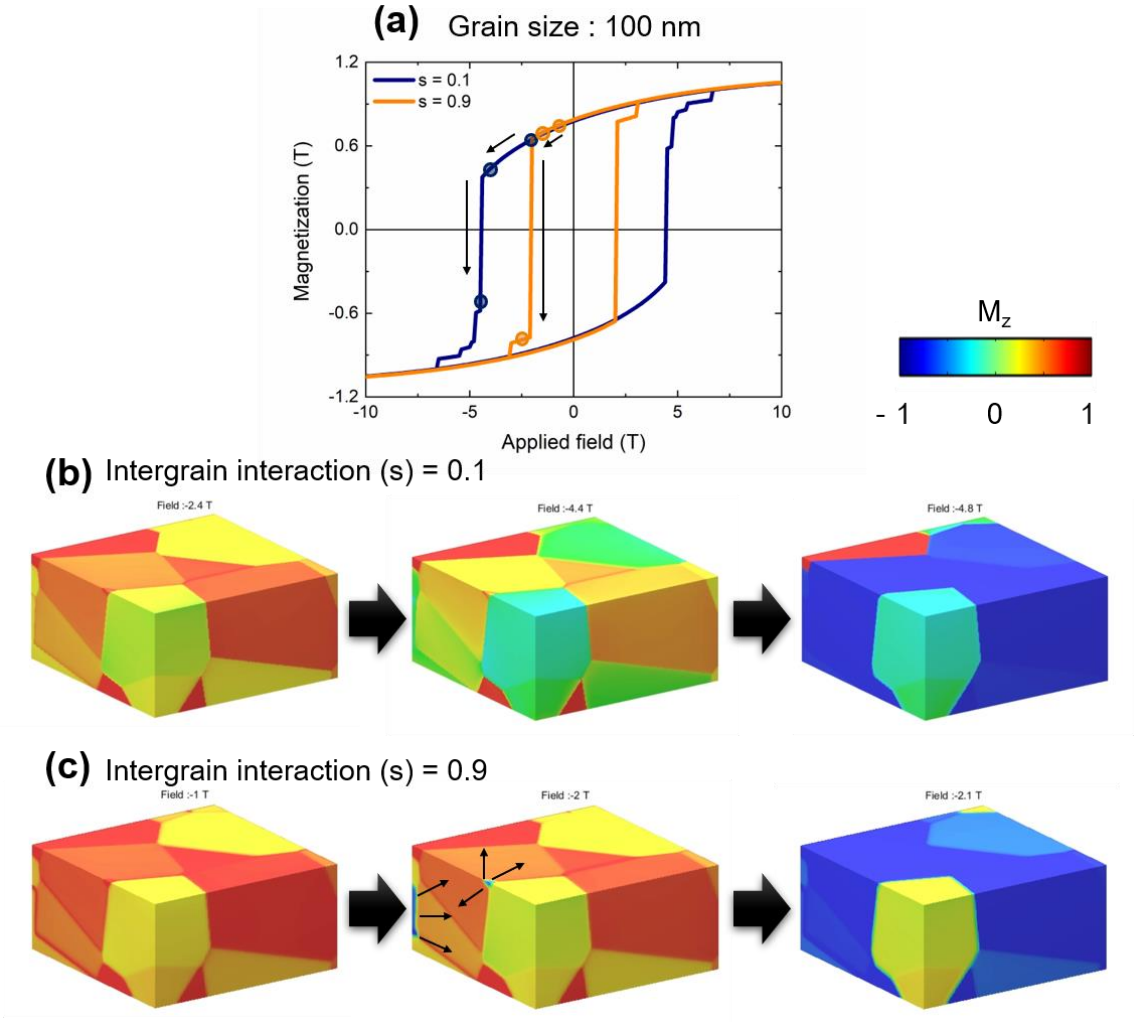

Figure 4.13 (a) Hysteresis loops of magnetization $\mu_0 M$ by applied magnetic field H_{app} for different intergrain exchange interaction of the model structure composed of 100 nm size grains. (b), (c) Schematic images of the magnetization along the z-axis (same direction with the easy axis). The grain structure is expressed in color according to the magnetization along z-axis, and the colored circle in (a) means each state of (b), (c).

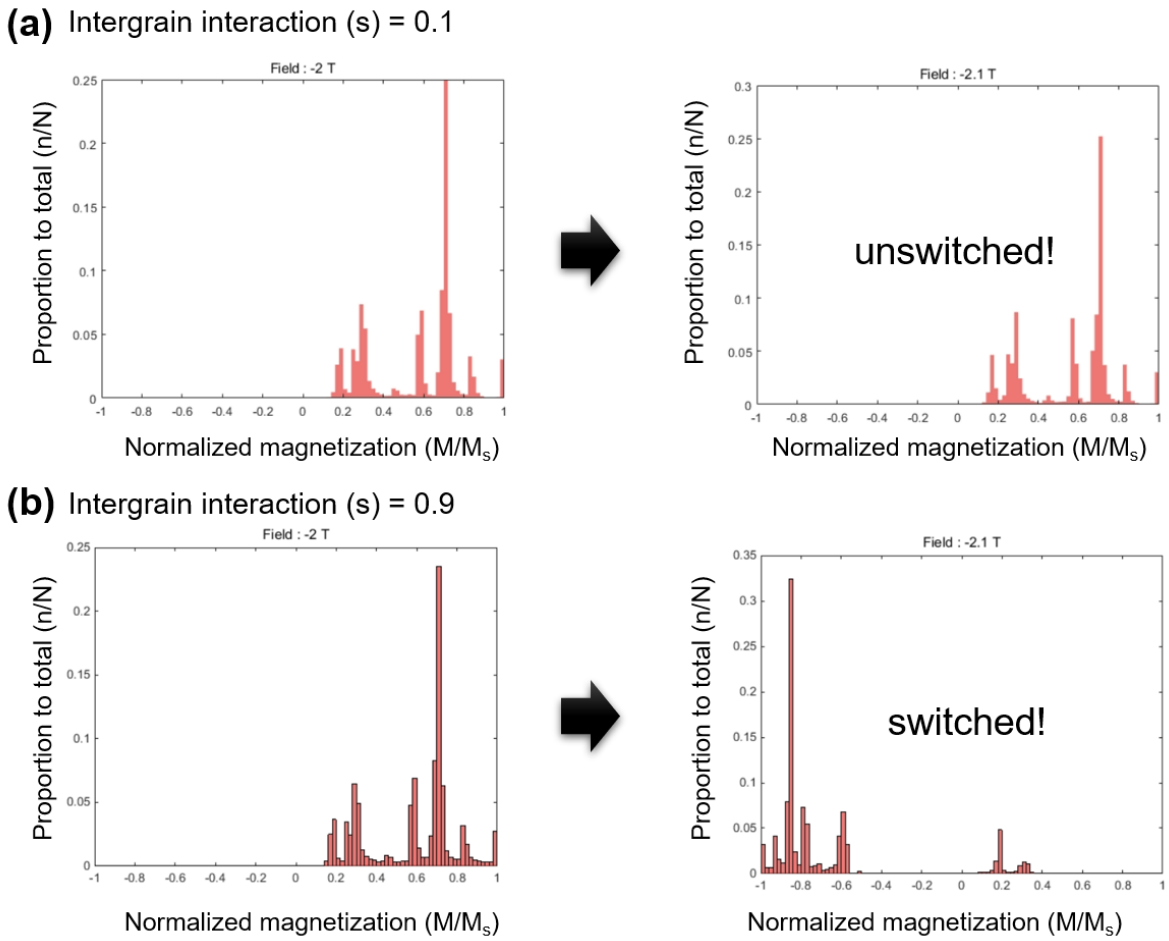

Figure 4.14 (a), (b) Histogram showing the proportion of the magnetization value in the z-axis direction to the whole material, which the value of the proportion is linearly proportional to the number of the magnetic moments having the value of the normalized magnetization.

4.4 Conclusion

To obtain a high energy product *BH*, the effect of the microstructure on the magnetic properties should be studied. In this chapter, various microstructures having different extrinsic properties have been investigated via micromagnetic simulations.

First of all, the degree of the anisotropy alignment is most important factor affecting the energy product, which the deviated angle follows as tan-type Gaussian distribution. When I compare the model systems having aligned microstructure with 0.9 degreed of alignment with randomly distributed microstructure, the energy product value is almost six times larger than the energy product of randomly distributed model.

The average size down of grains resulted in a high energy product value, as much of interfacial area of small grain size structure between grains disturbs the domain wall. By lowering the intergrain exchange interaction between neighboring grains, I obtained a high energy product value with much larger coercivity. The results reveal that the controlling the interface quality critically affects the coercivity, which can result in increasing stability of the magnet regardless the defects or the secondary phase for high energy product.

5. Exchange-coupled Cylindrical Core/Shell Structure

Exchange-coupled magnets are prominent candidates because they can exploit the advantages of both soft and hard-magnetic materials [54]–[60]. They also require a lesser amount of expensive rare earth elements. These magnets can attain high magnetic energies owing to the exchange coupling between the high-anisotropy hard-magnetic phase and the high-saturation-magnetization soft-magnetic phase.

Magnetic energy is represented by the energy product *BH*, which is twice the energy stored in the stray field outside the magnet. As noted by Skomski and Coey et al. [61]–[63], $(BH)_{max}$ should be evaluated rigorously from the hysteresis loop by considering the exact working point, which is determined by the shape of the magnet. Particularly for semi-hard magnets such as Alnico [64], [65]and exchange-coupled magnets, the hysteresis loop varies significantly with the shape of the magnet. Thus, $(BH)_{max}$ cannot be estimated from the hysteresis loop of a magnet with a specific shape, such as a thin film or powder; rather, it should be obtained from the *BH* values at the remanent state for magnets with various shapes.

In exchange-coupled magnets, the shape of the magnet has a great influence on the *BH* because not only the demagnetizing factor changes but also the area of the interphase between soft and hard phase for exchange-coupling. There is a trade-off with exchange hardening which maintains high remanent magnetization (M_r) by overcoming the shape anisotropy of the optimal shape through the interfacial exchange-coupling with hard phase. Recently, various studies have been actively carried out to find the optimal shape of the exchange-coupled magnet including layer-by-layer [66]–[68], core/shell structure [69]–[75], and mixed phase [56], [63], [76]–[82]. Since the layer-by-layer structure has the advantage of high packing efficiency, but it has a low nucleation field owing to strong demagnetizing field and nucleation mode by the layered structure, many researchers have been focused on controlling nucleation by manipulating the interlayer exchange coupling or thickness of the soft phase. To obtain a high nucleation field through a large interface between soft and hard phase, the core/shell structure has been proposed. Very recently, cylindrical core/shell microstructure has been presented not only for high energy product value but also for high nucleation field, which is compared in Figure 5.1. In addition, cylindrical core/shell structure has a benefit for controlling its demagnetizing factor determining working point with the change of the aspect ratio.

In this study, we performed micromagnetic simulations on core/shell hard–soft exchange-coupled magnetic cylinder with various geometrical parameters and wide-ranging volume ratios of the hard-to-soft phase, and rigorously evaluated the *BH* values at a working point considering the demagnetizing field, which is determined by shape. We explored the optimal geometry for maximizing *BH* by first examining the effects of dimensional scaling and phase ratio on a single exchange-coupled cylinder. Then, we examined the effects of scaling and the aspect ratio of the shape on arrays of exchange-coupled cylinders, with consideration of the shape of the array structure.

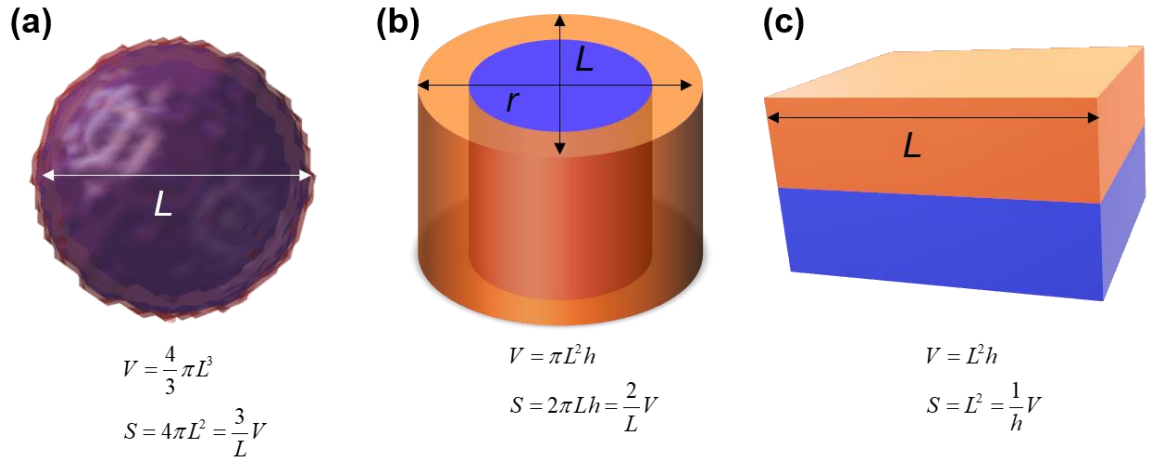

Figure 5.1 Volume and interfacial area of (a) sphere, (b) cylinder, (c) layer-by-layer structure for exchange-coupled magnet.

	Sphere	**Cylinder**	**Layer-by-layer**
Interfacial area	high	medium	low
Packing rate	low	medium	high
Demagnetizing factor	1/3	controllable	~1

Table 5.1 Comparison of interfacial area, packing rate, and demagnetizing factor of three types of exchange-coupled magnet.

5.1 Model System and Simulation Method

The exchange-coupled magnet model is illustrated in Figure 5.2. A cylindrical core/shell nanostructure with length L, consisting of a hard-magnetic core with diameter D surrounded by a soft-magnetic shell of thickness t is adopted. And I calculated the full hysteresis loop of the model using the finite differential micromagnetic solver MuMax3 [10]. We selected Sm_2Co_{17} as the hard-magnetic phase with an exchange stiffness $A_{ex,hard}$ of 1.4×10^{-11} J/m and saturation magnetization $M_{s,hard}$ of 1.034 MA/m^3. For the soft-magnetic phase, we selected FeCo with an exchange stiffness $A_{ex,soft}$ of 1.0×10^{-11} J/m and saturation magnetization $M_{s,soft}$ of 1.913 MA/m^3 [83]–[85]. In the finite differential calculation of the micromagnetic properties, a cubic cell of $2 \times 2 \times 2$ nm^3 was chosen, which was smaller than the exchange length of both phases. We assumed that the z-axis was the easy axis of magnetization of the hard-phase with a magnetocrystalline anisotropy constant of 3.3×10^6 J/m^3, whereas the soft-phase shell exhibited no crystalline anisotropy. We assumed perfect exchange coupling between the hard and soft phases with a harmonic mean value of A_{ex}/M_s for each phase. To obtain full hysteresis loops, an external magnetic field ranging from −10 to +10 T was applied along the easy axis. To obtain the correct BH values, we calculated mean value of the dot product of H and B in each cell.

To investigate the effect of the volume fraction of the high-magnetization soft phase on BH, we calculated the full hysteresis loops of the hard–soft core/shell cylinder with various shell thicknesses, t. To maximize the internal field H_d at remanence, we assumed that the hard core had dimensions of D = 48 nm and L = 24 nm.

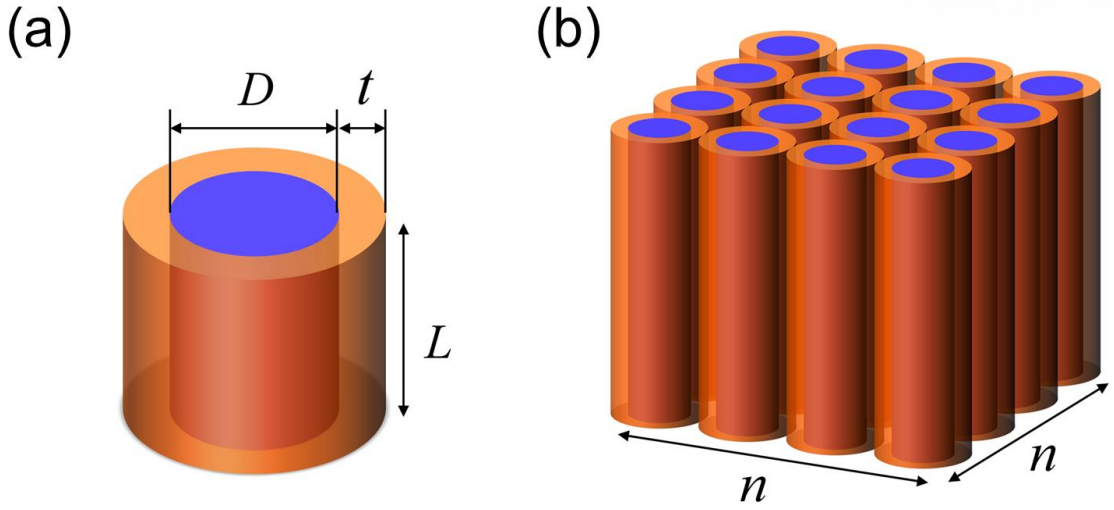

Figure 5.2 (a) Schematic of cylindrical core/shell structure with length L composed of hard-magnetic core with diameter D and soft-magnetic shell with thickness t. (b) Schematic of $n \times n$ array of cylindrical core/shell structures with 2 nm intervals between the cylinders.

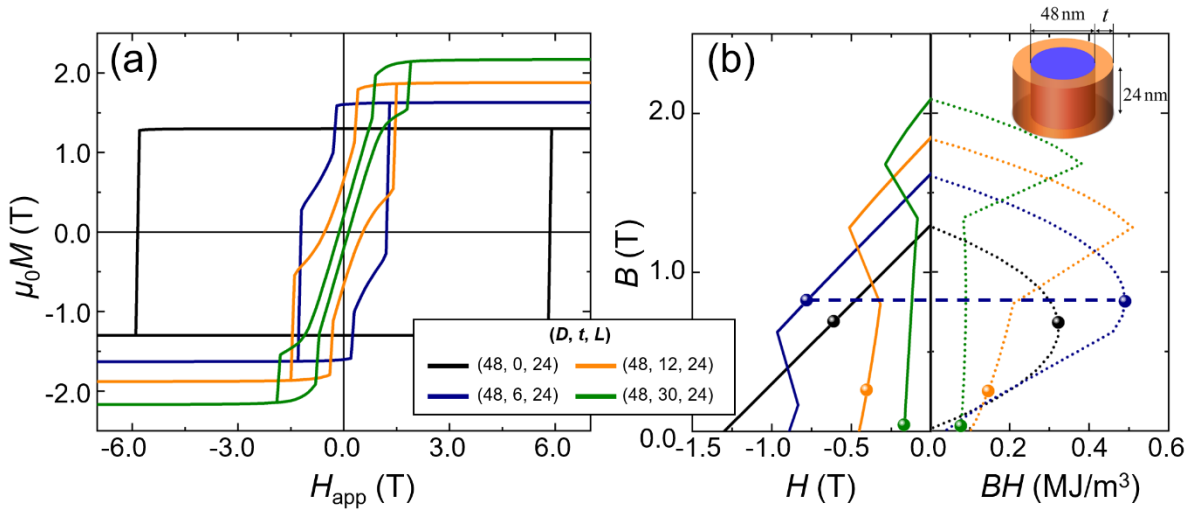

Figure 5.3 (a) Hysteresis loops of magnetization $\mu_0 M$ by applied magnetic field H_{app} for different thickness (t) soft-magnetic shells. (b) Second quadrant of the B versus $H = H_{app} + H_d$ loop (left) and energy product BH (right) of cylindrical core/shell structure. The spherical markers indicate the magnetic flux considering the demagnetization field H_d when $H_{app} = 0$. The dotted lines on the right side of the graph are not meaningful, except the working points.

5.2 Simulation Results

As depicted in Figure 5.3 (a), the saturation magnetization M_s increases in proportion to the volume fraction of the high-magnetization soft-phase, fs, according to the equation $M_s = (1 - f_s)M_{s,hard} + f_sM_{s,soft}$. However, the remanent magnetization M_r decreases suddenly when fs exceeds 0.33 (t = 6 nm). As a result, *BH* also falls abruptly. Because the soft phase exhibits no crystalline anisotropy, its magnetization switching depends on the balance between shape anisotropy and exchange hardening. Exchange hardening is inversely proportional to t; therefore, when the volume of the soft-magnetic phase is increased by increasing t, the shape anisotropy becomes more dominant than exchange hardening. Consequently, when t exceeds a critical value, the soft-magnetic phase does not follow the axis of the hard-magnetic phase owing to its shape anisotropy. For our model system, the critical value is 4 nm and thus hysteresis loops for t > 4 nm in Figure 5.3 (a) show two nucleation fields, which reveals that the soft phase starts to switch first followed by the hard phase. Hence, the negative nucleation field H_N of the soft-magnetic phase in the hysteresis loop can cause a sudden reduction in M_r.

Figure 5.3 (b) illustrates the second quadrant of the *B–H* loops (left-hand side, LHS) and the energy product *BH* (right-hand side, RHS) for core/shell magnets with different volume fractions of the soft-magnetic phase. The lines and symbols on the RHS represent the *BH* values and the working points at the remanent state for each geometry, respectively. To obtain the precise *BH* values, we integrated $B \cdot H$ in each cell for the whole volume instead of the conventional estimation derived from the area in the second quadrant of the *B–H* loop. There is a clear difference between *BH* calculated in two different ways. For instance, the integrated *BH* at the working point for (D, t, L) = (48, 30, 24) as seen a green symbol in the RHS of Figure 5.3 (b) has nonzero value notwithstanding almost zero value of the area in the LHS of Figure 5.3 (b).

To estimate the effect of dimensional scaling on *BH*, we compared the hysteresis loops and *BH* values for various scales while maintaining $t = D/4$ and $L/D = 0.5$ (Figure 5.4 (a) and (b)). As the scale decreased, H_N moved in the positive direction. When D was reduced to 16 nm, H_N became positive, significantly increasing *BH* to 0.6934 MJ/m^3—twice the value for the hard-magnetic cylinder. This reveals that scaling has a significant effect on the balance between exchange hardening and shape anisotropy. Because shape anisotropy mainly depends on the aspect ratio of the shape, scaling down increases the dominance of exchange hardening. When reducing the scale of the magnet, the thickness of the soft-magnetic phase decreases proportionally to the scaling factor, whereas the soft-phase volume fraction (which determines the saturation magnetization) remains unchanged. As exchange hardening is inversely proportional to the thickness, it increases significantly in comparison with the shape anisotropy. Below a specific scale (D = 16 in Figure 5.4 (a)), HN becomes positive, which considerably increases M_r and enables *BH* to reach its maximum value.

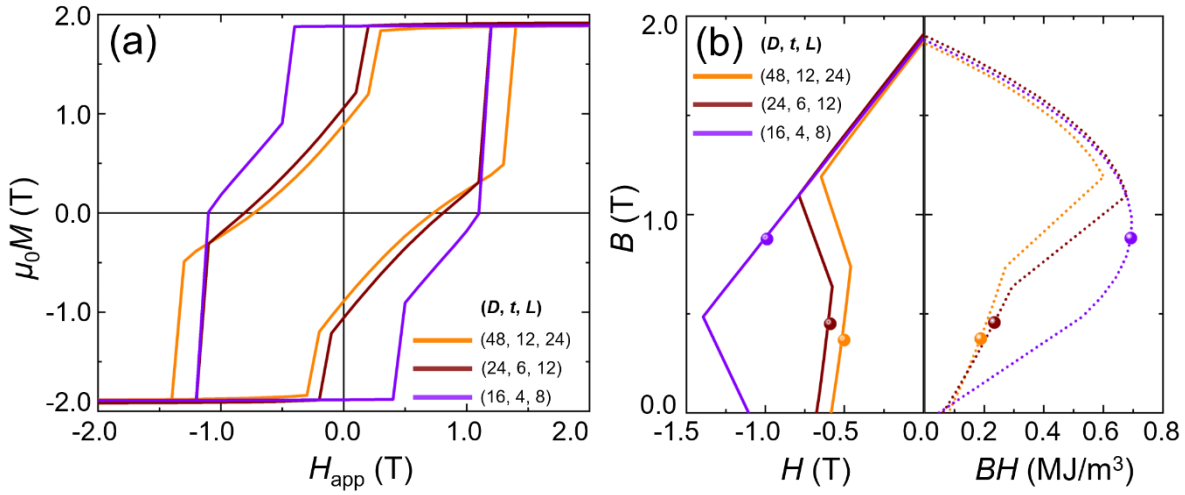

Figure 5.4 (a) $\mu_0 M$–H_{app} hysteresis loop of cylindrical core/shell structures with different scales. (b) Second quadrant of the B–H loop (left) and energy product BH (right) of cylindrical core/shell structures. The spherical markers indicate the magnetic flux considering the demagnetization field when the external field is zero.

The scaling effect can be clearly observed in the plots of BH vs. f_s in Figure 5.5 (a) for various values of D. At small values of f_s, the BH plots follows the theoretical increment of $(BH)_{max}$ (dashed line) because of the enhancement of the saturation magnetization according to the equation $(BH)_{max} = 1/2\ \mu_0(M_s)^2$. However, as fs increases above a critical value, BH suddenly decreases. The fs value at which the plot deviates from the theoretical estimation depends on the scale of the magnet; the larger the scale, the lower the critical value of fs. Figure 5.5 (b) depicts the plots of H_N vs. f_s, in which the critical f_s value is directly related to the sign of the nucleation field. This indicates that it is crucial to maximize the soft-magnetic phase fraction as much as possible while keeping H_N positive. Consequently, a smaller-scale system that follows the theoretical $(BH)_{max}$ estimation up to a higher soft-phase fraction can result in a higher BH.

As mentioned in the previous paragraph, we demonstrated that a positive nucleation field is essential for achieving a viable exchange-coupled nanostructure magnet with a high BH. Moreover, a positive H_N can be attained by scaling down the size of the magnet. Nevertheless, scaling down may limit the design flexibility or feasibility of scalable fabrication. To address this problem, we considered an array of nanostructured exchange-coupled magnets, similar to Alnico magnets or packed structures[64], [86], [87]. The array structure enables the magnet to be scaled up while maintaining the dominance of exchange hardening within each element. In this manner, by varying the aspect ratio of the elements, the shape anisotropy may assist exchange hardening.

First, we explored the effect of the aspect ratio (L/D) of a single exchange-coupled nanostructure magnet. When $L/D < 1.0$, the easy axis by exchange hardening is perpendicular to that of shape anisotropy; hence, there is competition between them. However, as L increases, the easy axis of shape anisotropy aligns with that of exchange hardening, which enables the soft-magnetic phase to fully couple with the hard-magnetic phase, resulting in the hysteresis loops illustrated in Figure 5.7 (a) and (b). In particular, for the case of $D = 24$ in Figure 5.7 (b), the negative H_N value becomes positive as L increases. Figure 5.7 (c) depicts the variation in H_N with the aspect ratio L/D at different scales. All plots demonstrate a similar trend with the shape-anisotropy energy for an ellipsoid or cylinder, but with different offsets depending on the scaling. This is because exchange hardening depends on the scaling, whereas shape anisotropy does not. Interestingly, when $D = 48$ nm, H_N does not become positive even at significantly high values of L/D, although it is expected to be positive based on the coupling of shape anisotropy and exchange hardening. This reveals that there is an additional scaling-dependent factor for determining H_N; that is, the nucleation mode is affected by the scale. As the system size increases, the nucleation mode changes from a coherent rotation mode to curling or a more complicated mode.

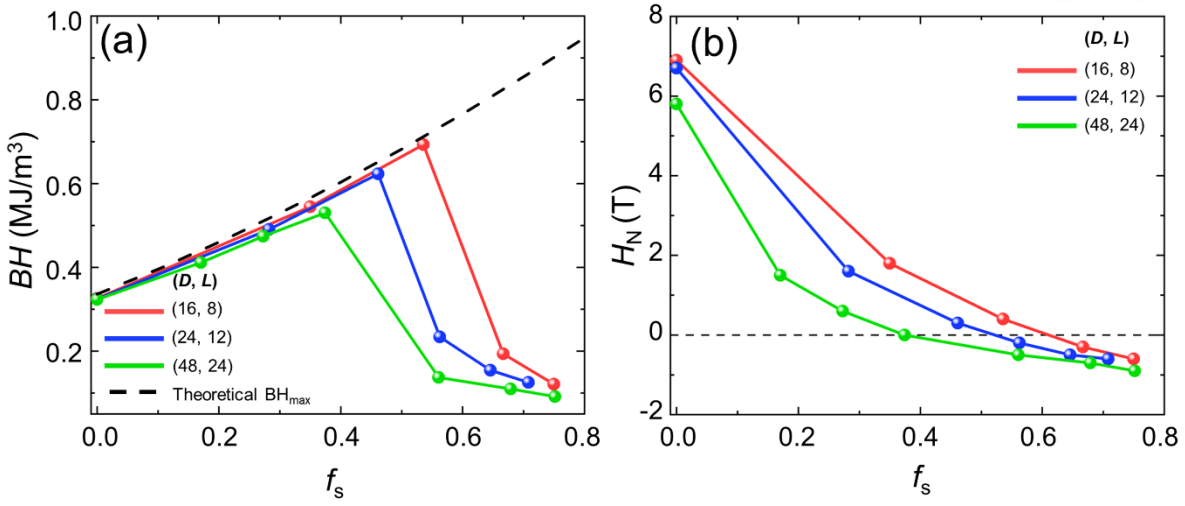

Figure 5.5 (a) Energy product *BH* as a function of the soft-phase volume fraction f_s at different scales. The dashed black line represents the theoretical $(BH)_{max}$ according to f_s. (b) Nucleation field H_N of cylindrical core/shell structures as a function of f_s at different scales.

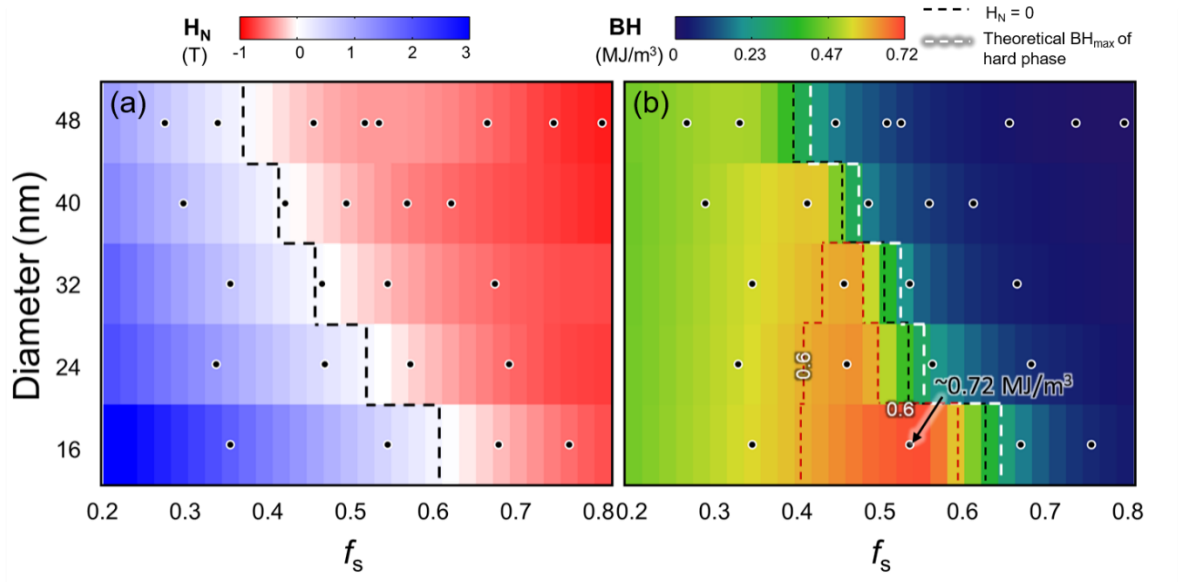

Figure 5.6 Diameter of the hard-magnetic core-fraction of the soft magnetic shell phase diagram. (a) The nucleation field (H_N) from simulation results is plotted as black dots, and its color is linearly interpolated in each diameter. The black dashed line means that the calculated nucleation field is to be zero. (b) The energy product (*BH*) from simulation results is plotted as black dots, and its color is linearly interpolated in each diameter. The white dashed line indicates the theoretical maximum energy product of the hard phase.

Increasing the length reduces the internal field H_d, which results in a decrease in *BH* above 0.5*D*, as depicted in Figure 5.7 (d). Because *BH* only depends on the remanent state, the value of the nucleation field itself does not affect the value of *BH*, apart from changing *BH* when the sign changes. $(BH)_{max}$ cannot occur at aspect ratios that maximize H_d (for example, at aspect ratios of L/D = 1, 1.6, and 4.5, where D = 24, 40, and 48 nm, respectively) due to the nucleation mode, as shown in Figure 5.7 (d).

To scale up the nanostructured exchange-coupled magnet, we assume a simple array of $n \times n$ core/shell cylinders with 2 nm intervals between the cylinders, as illustrated in Figure 5.2 (b). Each cylinder is free from exchange coupling. Arrays of unit cylinders with geometries of (D, t, L) = (16, 4, 144) and (24, 6, 216) are considered, with both having a positive H_N value according to Figure 5.7 (c). Figure 5.8 (a) depicts the variation in *BH* according to the array size n. Increasing the lateral dimension n increases *BH* by maximizing the internal field H_d. Because the cylindrical units have the same aspect ratio but a different scale, they may be expected to demonstrate the same *BH* dependence on n. However, $(BH)_{max}$ is dependent on the unit geometry. With unit cylinder dimensions of (D, t, L) = (16, 4, 144), *BH* increases continually to 0.6554 MJ/m^3 at n = 25; when (D, t, L) = (24, 6, 216), *BH* reaches a maximum of 0.4559 MJ/m^3 at n = 6 and then falls rapidly as H_N becomes negative at n > 6 (Figure 5.8 (b)). This may be due to the dipole–dipole interactions among the unit cylinders in the array structure, which reduce the shape anisotropy of the unit cylinders and give rise to nonuniform cylinder-by-cylinder switching in the array structure. On the other hand, in the case of the array composed with unit cylinder of (D, t, L) = (16, 4, 144), the exchange hardening overcomes dipole–dipole interaction until n = 40 with periodic boundary condition, and the H_N keeps positive, which results in the *BH* follows quadratic function maximized at $H_d = 1/2M_s$.

The results reveal that scaled-up bulk magnets can be fabricated through array structures of hard–soft exchange-coupled cylindrical magnets. In addition, the *BH* can be maximized by designing unit nanostructures with an optimal geometry and arranging them in an optimal array structure, with consideration of the sign of the nucleation field resulting from exchange hardening and shape anisotropy, as well as the shape anisotropy of the bulk structure due to dipole–dipole interactions among the unit structures.

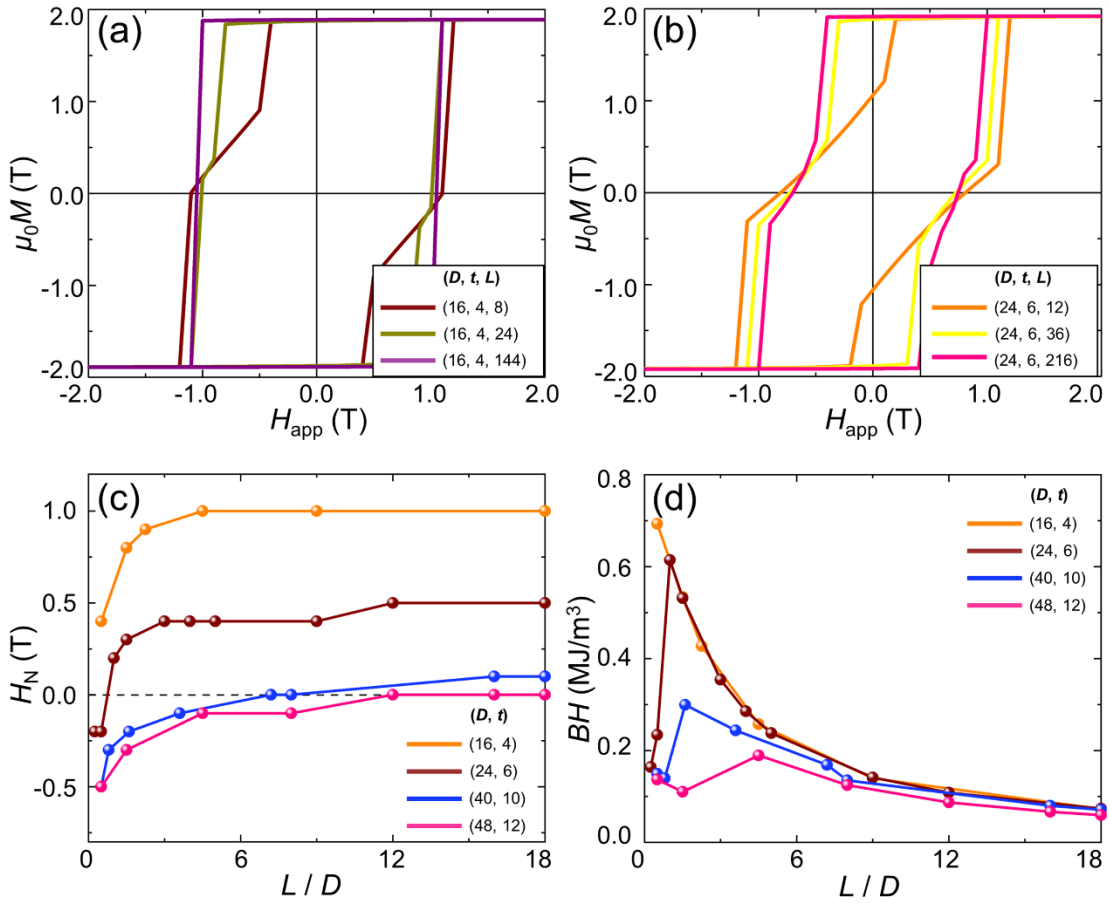

Figure 5.7 $\mu_0 M$–H_{app} hysteresis loops of magnetization for magnets with (a) (D, t) = (16, 4) and (b) (D, t) = (24, 6) for different lengths (L). (c) Nucleation field H_N and (d) energy product BH of cylindrical core/shell structures as a function of the aspect ratio (L/D).

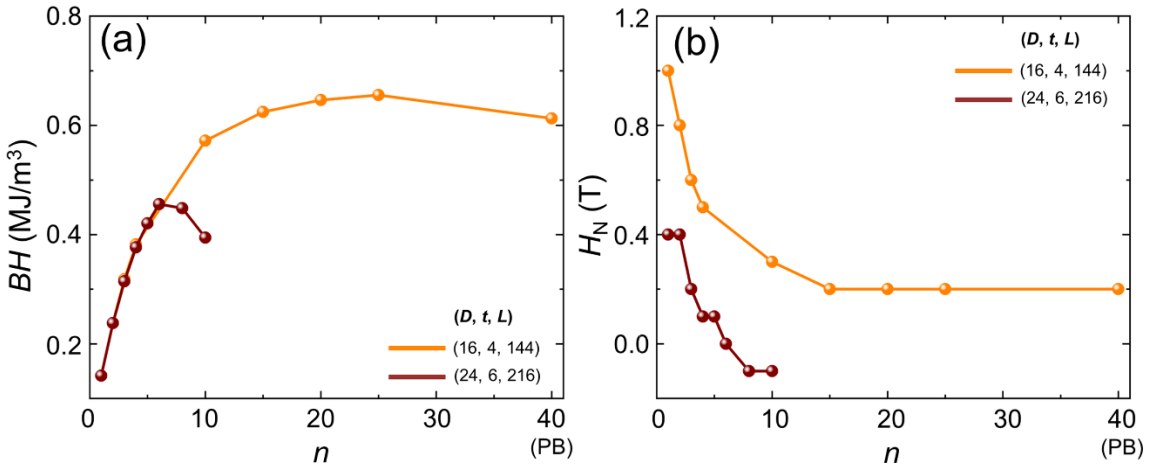

Figure 5.8 (a) Energy product BH and (b) nucleation field H_N of cylindrical core/shell structure arrays as a function of n. In array structure of 40 × 40, the periodic boundary condition (PB) is applied along the x and y axes, not along the z axis.

5.3 Conclusion

To obtain a high energy product *BH*, various geometries of cylindrical core/shell hard–soft exchange-coupled magnetic nanostructures have been investigated via micromagnetic simulations. The scaling down of the nanostructure resulted in a high *BH* value, as a high volume-fraction of the soft-magnetic phase could be attained while maintaining a positive nucleation field by exchange hardening. I demonstrated that this nanostructured magnet could be scaled up by preparing an array of exchange-coupled cylinders. By creating needle-shaped nanostructured units and increasing the size of the array, I obtained a high *BH* value on a large scale. The results reveal the theoretical possibility of nanostructured exchange-coupled magnets, establish guidelines for design flexibility, and demonstrate the feasibility of scalable fabrication of bulk magnets with arrays of exchange-coupled nanostructures.

6. Summary

As the trend of energy conversion changes from internal combustion engine to motor that converts electrical energy into kinetic energy, the importance of permanent magnets playing a key role in the motor is increasing in recent year. To develop high performance permanent magnet, many studies have been conducted to increase coercive force of a magnet maintaining stability and having high energy product. Since the microstructure of the magnet plays a key role in determining the coercivity and the energy product as extrinsic properties of the magnet. Since there are clearly experimental limitations in measuring magnetic field, in order to make a good permanent magnet, an accurate understanding of magnets and magnetism is essential. In this thesis, the influence of various microstructures on magnetic properties and the modeling of microstructures using them were studied via micromagnetic simulation.

The energy product *BH* is the figure-of-merit, which is twice the energy stored in the stray field outside the magnet. It can be obtained from the volume integral of the square of the stray field outside the magnet, or from the volume integral of the dot product between the demagnetizing field H_d and the internal magnetic flux density *B*. In the case of a general magnetic material, if the magnetic anisotropy energy of the magnet is not sufficiently large, the remanent magnetization (M_r) is not the same as the saturation magnetization (M_s) according to various extrinsic factors such as microstructure, and the hysteresis curve $M(H_{app})$ changes sensitively according to the shape of the magnet. Thus, the practical energy product cannot be predicted without considering the demagnetizing field inside the magnet, it is necessary to derive the maximum energy product by making various shapes of the magnetic material.

From micromagnetic simulation of the modeled microstructure having constraint extrinsic properties such as degree of the grain anisotropy alignment, system shape, grain size, and intergrain exchange interaction, all the extrinsic properties influence the hysteresis of the magnet in complex combination. Especially, the degree of the grain anisotropy alignment determined from post-treatment process when manufacturing magnets is directly related to the remanent magnetization M_r, which results in the energy product at the remanent state. In addition, the smaller the average grain size under the single domain size of the material, the higher energy product due to its strong nucleation field, which comes from the size effect of the magnet and pinning of the domain wall propagation during the reversal process. With maximizing this pinning phenomenon at the interface, the low intergrain exchange interaction makes the nucleation field of the magnet large. In experiment, this decoupling of each grain can be enhanced by creating nonmagnetic materials at the grain boundary.

Finally, the exchange-coupled cylindrical core/shell magnet is investigated to obtain high energy product by combining hard and soft magnetic materials. The scaling down of the nanostructure causes a high *BH* value, as a high volume-fraction of the soft-magnetic phase could be attained while maintaining a positive nucleation field by exchange hardening. I demonstrated that this nanostructured magnet could be scaled up by preparing an array of exchange-coupled cylinders. By creating needle-

shaped nanostructured units and increasing the size of the array, I obtained a high *BH* value on a large scale. The results reveal the theoretical possibility of nanostructured exchange-coupled magnets, establish guidelines for design flexibility, and demonstrate the feasibility of scalable fabrication of bulk magnets with arrays of exchange-coupled nanostructures.

From the studies for enhancing the energy product, many of extrinsic properties have been understood and prominent model system as exchange-coupled magnet is also proposed. However, there is still discrepancy between the experimental results and the simulation results of the modeled magnetic system, and there are also limits to the size of the micromagnetic simulation. To further reduce the discrepancy, the combination of statistics and the micromagnetic simulation will be developed for predicting the bulk sized magnetic properties. In addition, through the analysis of the hysteresis loop resulting from the experiment, new model that can predict the microstructure of the magnet and suggest the direction of the manufacturing process will be established.

References

[1] J. M. D. Coey, "PERMANENT MAGNETISM," *Solid State Commun.*, vol. 102, no. 2–3, pp. 101–105, 1997.

[2] O. Gutfleisch, M. A. Willard, E. Brück, C. H. Chen, S. G. Sankar, and J. P. Liu, "Magnetic materials and devices for the 21st century: Stronger, lighter, and more energy efficient," *Adv. Mater.*, vol. 23, no. 7, pp. 821–842, 2011.

[3] N. Poudyal and J. Ping Liu, "Advances in nanostructured permanent magnets research," *J. Phys. D. Appl. Phys.*, vol. 46, p. 043301, 2013.

[4] R. W. McCallum, L. Lewis, R. Skomski, M. J. Kramer, and I. E. Anderson, "Practical Aspects of Modern and Future Permanent Magnets," *Annu. Rev. Mater. Res.*, vol. 44, pp. 451–477, 2014.

[5] S. M. Lu, "A review of high-efficiency motors: Specification, policy, and technology," *Renew. Sustain. Energy Rev.*, vol. 59, pp. 1–12, 2016.

[6] D. Li, D. S. Pan, S. J. Li, and Z. D. Zhang, "Recent developments of rare-earth-free hard-magnetic materials," *Sci. China Physics, Mech. Astron.*, vol. 59, no. 1, pp. 1–17, 2016.

[7] S. Hirosawa, M. Nishino, and S. Miyashita, "Perspectives for high-performance permanent magnets : applications , coercivity , and new materials *," *Adv. Nat. Sci. Nanosci. Nanotechnol.*, p. aa597c, 2017.

[8] K. Hono and H. Sepehri-Amin, "Prospect for HRE-free high coercivity Nd-Fe-B permanent magnets," *Scr. Mater.*, vol. 151, pp. 6–13, 2018.

[9] D. Goll, *Micromagnetism–Microstructure Relations and the Hysteresis Loop*, vol. 5. 2007.

[10] A. Vansteenkiste, J. Leliaert, M. Dvornik, M. Helsen, F. Garcia-Sanchez, and B. Van Waeyenberge, "The design and verification of MuMax3," *AIP Adv.*, vol. 4, p. 107133, 2014.

[11] R. Skomski, *Simple Models of Magnetisim*. 2008.

[12] J. M. D. Coey., *Magnetism and magnetic materials*, no. 1. Cambridge : Cambridge University Press, 2010.

[13] N. C. Pop, "A model for magnetic hysteresis," *Eur. Phys. J. Plus*, vol. 134, no. 11, 2019.

[14] L. Tauxe, H. N. Bertram, and C. Seberino, "Physical interpretation of hysteresis loops: Micromagnetic modeling of fine particle magnetite," *Geochemistry, Geophys. Geosystems*, vol. 3, no. 10, 2002.

[15] R. Wood, "Exact solution for a Stoner-Wohlfarth particle in an applied field and a new approximation for the energy barrier," *IEEE Trans. Magn.*, vol. 45, no. 1, pp. 100–103, 2009.

[16] N. Kim, H.-S. Han, and K.-S. Lee, "A Limit to Predict Maximum Energy Product (BHmax) from the Magnetization Hysteresis Loop," *J. Korean Magn. Soc.*, vol. 28, no. 5, pp. 205–211, 2018.

[17] D. Givord and A. N. Dobrynin, “Demagnetising fields in assemblies of magnetostatically coupled Stoner-Wohlfarth particles,” *J. Magn. Magn. Mater.*, vol. 489, no. February, p. 165293, 2019.

[18] G. Herzer, “Grain Size Dependence of Coercivity and Permeability in Nanocrystalline Ferromagnets,” *IEEE Trans. Magn.*, vol. 26, no. 5, pp. 1397–1402, 1990.

[19] E. Cardelli, M. Carpentieri, A. Faba, and G. Finocchio, “Modeling of hysteresis in magnetic multidomains,” *Phys. B Condens. Matter*, vol. 435, pp. 62–65, 2014.

[20] J. Liu *et al.*, “Grain size dependence of coercivity of hot-deformed Nd-Fe-B anisotropic magnets,” *Acta Mater.*, vol. 82, pp. 336–343, 2015.

[21] L. Schultz, K. Schnitzke, J. Wecker, M. Katter, and C. Kuhrt, “Permanent magnets by mechanical alloying (invited),” *J. Appl. Phys.*, vol. 70, no. 10, pp. 6339–6344, 1991.

[22] T. Klemmer, D. Hoydick, H. Okumura, B. Zhang, and W. A. Soffa, “Magnetic Hardening and Coercitiy in L10 ordered FePd Ferromagents,” *Scr. Mater.*, vol. 33, pp. 1793–1805, 1995.

[23] H. Kronmüller, R. Fischer, M. Seeger, and A. Zern, “Micromagnetism and microstructure of hard magnetic materials,” *J. Phys. D. Appl. Phys.*, vol. 29, no. 9, pp. 2274–2283, 1996.

[24] O. Gutfleisch, “Controlling the properties of high energy density permanent magnetic materials by different processing routes,” *J. Phys. D. Appl. Phys.*, vol. 33, no. 17, 2000.

[25] J. Fidler and T. Schrefl, “Micromagnetic modelling - The current state of the art,” *J. Phys. D. Appl. Phys.*, vol. 33, no. 15, 2000.

[26] R. Skomski, “Nanomagnetics,” *J. Phys. Condens. Matter*, vol. 15, 2003.

[27] M. F. De Campos, “Effect of grain size, lattice defects and crystalline orientation on the coercivity of sintered magnets,” *Mater. Sci. Forum*, vol. 530–531, pp. 146–151, 2006.

[28] W. B. Cui, Y. K. Takahashi, and K. Hono, “Microstructure optimization to achieve high coercivity in anisotropic Nd-Fe-B thin films,” *Acta Mater.*, vol. 59, no. 20, pp. 7768–7775, 2011.

[29] T. Kawai, B. M. Ma, S. G. Sankar, and W. E. Wallace, “Effect of crystal alignment on the remanence of sintered NdFeB magnets,” *J. Appl. Phys.*, vol. 67, no. 9, pp. 4610–4612, 1990.

[30] R. Gao, W. Li, J. Zhang, L. Wu, and X. Yu, “Effects of orientation and interaction of grains on coercivity for sintered NdFeB magnets,” *Sci. China, Ser. A Math. Physics, Astron.*, vol. 42, no. 6, pp. 653–659, 1999.

[31] S. Sato, S. J. Lee, C. Mitsumata, H. Yanagihara, and E. Kita, “Random magnetic anisotropy in isotropic nanocrystalline composite permanent magnets,” *J. Appl. Phys.*, vol. 109, no. 8, 2011.

[32] Y. Matsuura, N. Kitai, S. Hosokawa, and J. Hoshijima, “Relation between the alignment dependence of coercive force decrease ratio and the angular dependence of coercive force of ferrite magnets,” *J. Magn. Magn. Mater.*, vol. 411, pp. 1–6, 2016.

[33] Y. Matsuura, N. Kitai, R. Ishii, T. Natsumeda, and J. Hoshijima, "Recoil curve properties and coercive force decrease ratio in NdFeB sintered magnets," *J. Magn. Magn. Mater.*, vol. 346, pp. 113–117, 2013.

[34] Y. Matsuura, J. Hoshijima, and R. Ishii, "Relation between Nd 2 Fe 14 B grain alignment and coercive force decrease ratio in NdFeB sintered magnets," *J. Magn. Magn. Mater.*, vol. 336, pp. 88–92, 2013.

[35] R. W. Gao, D. H. Zhang, H. Li, and J. C. Zhang, "Effects of the degree of grain alignment on the hard magnetic properties of sintered NdFeB magnets," *Appl. Phys. A*, vol. 67, pp. 353–356, 1998.

[36] T. Ohkubo, H. Sepehri-Amin, and K. Hono, "Micromagnetic Simulations of Magnetization Reversals in Nd-Fe-B Based Permanent Magnets," *Nippon Kinzoku Gakkaishi/Journal Japan Inst. Met.*, vol. 81, no. 1, pp. 11–18, 2017.

[37] J. Fischbacher *et al.*, "Micromagnetics for the coercivity of nanocomposite permanent magnets," *Int. Work. Rare Earth Futur. Perm. Magnets Their Appl.*, no. January 2015, 2014.

[38] S. Bance, J. Fischbacher, T. Schrefl, I. Zins, G. Rieger, and C. Cassignol, "Micromagnetics of shape anisotropy based permanent magnets," *J. Magn. Magn. Mater.*, vol. 363, no. March, pp. 121–124, 2014.

[39] J. Fujisaki *et al.*, "Micromagnetic Simulations of Magnetization Reversal in Misaligned Multigrain Magnets With Various Grain Boundary Properties Using Large-Scale Parallel Computing," *IEEE Trans. Magn. VOL. 50*, vol. 50, no. 11, 2014.

[40] D. Yao, S. Ge, X. Zhou, and H. Zuo, "Grain size dependence of coercivity in magnetic metal-insulator nanogranular films with uniaxial magnetic anisotropy," *J. Appl. Phys.*, vol. 107, no. 7, 2010.

[41] S. Li *et al.*, "Role of amorphous grain boundaries in nanocomposite NdFeB permanent magnets," *J. Appl. Phys.*, vol. 92, no. 12, pp. 7514–7518, 2002.

[42] X. K. Sun, J. Zhang, Y. Chu, W. Liu, B. Cui, and Z. Zhang, "Dependence of magnetic properties on grain size of α-Fe in nanocomposite (Nd, Dy)(Fe, Co, Nb, B)5.5/α-Fe magnets," *Appl. Phys. Lett.*, vol. 74, no. 12, pp. 1740–1742, 1999.

[43] M. Menarini *et al.*, "Micromagnetic simulator for complex granular systems based on Voronoi tessellation," *J. Magn. Magn. Mater.*, vol. 482, no. March, pp. 350–357, 2019.

[44] G. Ding *et al.*, "Coercivity enhancement in Dy-free sintered Nd-Fe-B magnets by effective structure optimization of grain boundaries," *J. Alloys Compd.*, vol. 735, pp. 795–801, 2018.

[45] T. H. Kim *et al.*, "Microstructure of a Dy-free Nd-Fe-B sintered magnet with 2 T coercivity," *Acta Mater.*, vol. 156, pp. 146–157, 2018.

[46] A. Kovacs *et al.*, "Micromagnetic Simulations for Coercivity Improvement Through Nano-

Structuring of Rare-Earth-Free L10-FeNi Magnets," *IEEE Trans. Magn.*, vol. 53, no. 11, 2017.

[47] A. Müller, "Magnetic material R,Fe,Mo,(Co) with ThMn12 structure," *J. Appl. Phys.*, vol. 64, no. 1, pp. 249–251, 1988.

[48] A. Hütten and G. Thomas, "Coercivity mechanism in SmFeTi rare-earth magnets," *J. Appl. Phys.*, vol. 70, no. 10, pp. 6113–6115, 1991.

[49] T. Saito, H. Miyoshi, and D. Nishio-Hamane, "Magnetic properties of Sm-Fe-Ti nanocomposite magnets with a ThMn 12 structure," *J. Alloys Compd.*, vol. 519, pp. 144–148, 2012.

[50] A. M. Gabay and G. C. Hadjipanayis, "ThMn12-type structure and uniaxial magnetic anisotropy in ZrFe10Si2 and Zr1-xCexFe10Si2 alloys," *J. Alloys Compd.*, vol. 657, pp. 133–137, 2016.

[51] H. Fukunaga and H. Inoue, "Effect of Intergrain Exchange Interaction on Magnetic Properties in Isotropic Nd-Fe-B Magnets," *Jpn. J. Appl. Phys.*, vol. 31, no. 5 R, pp. 1347–1352, 1992.

[52] H. W. Zhang *et al.*, "Intergrain exchange coupling and coercivity mechanism of nanocrystalline Sm2Fe15-xCuxSi2C(x=0 and 1) ribbons prepared by melt spinning," *Phys. Rev. B - Condens. Matter Mater. Phys.*, vol. 60, no. 1, pp. 64–67, 1999.

[53] R. Fischer and H. Kronmüller, "The role of the exchange interaction in nanocrystalline isotropic Nd2Fe14B-magnets," *J. Magn. Magn. Mater.*, vol. 191, no. 1–2, pp. 225–233, 1999.

[54] S. K. Sharma, *Complex Magnetic Nanostructures*. 2017.

[55] A. Morelos-Gómez *et al.*, "Controlling high coercivities of ferromagnetic nanowires encapsulated in carbon nanotubes," *J. Mater. Chem.*, vol. 20, no. 28, pp. 5906–5914, 2010.

[56] E. E. Fullerton, J. S. Jiang, and S. D. Bader, "Hard/soft magnetic heterostructures: model exchange-spring magnets," *J. Magn. Magn. Mater.*, vol. 200, no. 1–3, pp. 392–404, 1999.

[57] R. Skomski and J. M. D. Coey, "Nucleation field and energy product of aligned two-phase magnets - progress towards the '1 MJ/m3' magnet," *IEEE Trans. Magn.*, vol. 29, no. 6, pp. 2860–2862, 1993.

[58] R. Skomski and J. M. D. Coey, "Giant energy product in nanostructured two-phase magnets," *Phys. Rev. B*, vol. 48, no. 21, pp. 15812–15816, 1993.

[59] E. F. Kneller and R. Hawig, "The exchange-spring magnet: A new material principle for permanent magnets," *IEEE Trans. Magn.*, vol. 27, no. 4, pp. 3588–3600, 1991.

[60] W. Schartl, "Current directions in core – shell nanoparticle design †," *Nanoscale*, vol. 2, pp. 829–843, 2010.

[61] A. L. Wysocki and V. P. Antropov, "Micromagnetic simulations with periodic boundary conditions : Hard-soft nanocomposites," *J. Magn. Magn. Mater.*, vol. 428, pp. 274–286, 2017.

[62] R. Skomski and J. M. D. Coey, "Magnetic anisotropy — How much is enough for a permanent

magnet ?," *Scr. Mater.*, vol. 112, pp. 3–8, 2016.

[63] Y. Shen, S. O. Leontsev, Z. Turgut, M. S. Lucas, A. O. Sheets, and J. C. Horwath, "Effect of soft phase on magnetic properties of bulk Sm-Co/α-Fe nanocomposite magnets," *IEEE Trans. Magn.*, vol. 49, no. 7, pp. 3244–3247, 2013.

[64] R. Skomski, Y. Liu, J. E. Shield, G. C. Hadjipanayis, and D. J. Sellmyer, "Permanent magnetism of dense-packed nanostructures," *J. Appl. Phys.*, vol. 107, no. 9, p. 351, 2010.

[65] L. Ke *et al.*, "Simulation of alnico coercivity," *Appl. Phys. Lett.*, vol. 111, no. 022403, pp. 1–5, 2017.

[66] W. B. Cui *et al.*, "Exchange coupling in hard/soft-magnetic multilayer films with non-magnetic spacer layers," *J. Appl. Phys.*, vol. 111, no. 7, pp. 1–4, 2012.

[67] Y. Liu *et al.*, "Magnetic structure in Fe/Sm-Co exchange spring bilayers with intermixed interfaces," *Phys. Rev. B - Condens. Matter Mater. Phys.*, vol. 83, no. 17, pp. 1–7, 2011.

[68] R. Mandal *et al.*, "Time domain magnetization dynamics study to estimate interlayer exchange coupling constant in Nd-Fe-B/Ni80Fe20 films," *J. Magn. Magn. Mater.*, vol. 468, no. May, pp. 273–278, 2018.

[69] J. Lee *et al.*, "Exchange-Coupling Interaction in Zero- and One-Dimensional Sm 2 Co 17 /FeCo Core − Shell Nanomagnets," *ACS Appl. Mater. Interfaces*, vol. 11, pp. 26222–26227, 2019.

[70] E. Lottini *et al.*, "Strongly Exchange Coupled Core|Shell Nanoparticles with High Magnetic Anisotropy: A Strategy toward Rare-Earth-Free Permanent Magnets," *Chem. Mater.*, vol. 28, no. 12, pp. 4214–4222, 2016.

[71] A. López-ortega, M. Estrader, and G. Salazar-alvarez, "Applications of exchange coupled bi-magnetic hard / soft and soft / hard magnetic core / shell nanoparticles," *Phys. Rep.*, vol. 553, pp. 1–32, 2015.

[72] J. S. Jiang, "Magnetization processes in core/shell exchange-spring structures," *J. Appl. Phys.*, vol. 117, p. 17A734, 2015.

[73] P.-O. Jubert, "Micromagnetic Simulations of Exchange-Coupled Core-Shell Particulate Media," *IEEE Trans. Magn.*, vol. 50, no. 11, p. 3002004, 2014.

[74] R. G. Chaudhuri and S. Paria, "Core / Shell Nanoparticles : Classes , Properties , Synthesis Mechanisms , Characterization , and Applications," *Chem. Rev.*, vol. 112, pp. 2373–2433, 2012.

[75] H. Fukunaga, R. Horikawa, M. Nakano, T. Yanai, T. Fukuzaki, and K. Abe, "Computer Simulations of the Magnetic Properties of Nanocomposite Magnets With a Core-Shell Structure," *IEEE Trans. Magn.*, vol. 49, no. 7, pp. 3240–3243, 2013.

[76] T. Saito and H. Miyoshi, "Magnetic properties of Sm 5Fe 17/Fe composite magnets produced

by spark plasma sintering method," *J. Appl. Phys.*, vol. 111, no. 7, pp. 109–112, 2012.

[77] A. Chakraborty, R. Hirian, G. Kapun, and V. Pop, "Magnetic Properties of SmCo 5 + 10 wt % Fe Exchange-Coupled Nanocomposites Produced from Recycled SmCo 5," *nanomaterials*, vol. 10, no. 7, p. 1308, 2020.

[78] R. R. Alexander and R. J. Joseyphus, "Effect of microstructure parameter on the energy product in two-phase permanent magnetic materials," *Mod. Phys. Lett. B*, vol. 1950025, 2019.

[79] H. Ryo, L. Hu, J. Kim, and Y. Yang, "Micromagnetic Study for Magnetic Properties of Exchange-Coupled Nanocomposite Magnetic Systems With α -Fe Grains Embedded in Nd 2 Fe 14 B Matrix," *IEEE Trans. Magn.*, vol. 53, no. 2, p. 7400207, 2017.

[80] H. Zeng, J. Li, J. P. Liu, Z. L. Wang, and S. Sun, "Exchange-coupled nanocomposite magnets by nanoparticle," *Nature*, vol. 420, pp. 395–398, 2002.

[81] Z. C. Wang, H. A. Davies, S. Z. Zhou, M. C. Zhang, and Y. Qiao, "Preparation and magnetic properties of melt-spun Nd 2Fe 14(BC)/α-Fe nanocomposite magnets," *J. Appl. Phys.*, vol. 91, no. 10 I, pp. 7884–7886, 2002.

[82] D. Liu *et al.*, "Computational analysis of microstructure- coercivity relation in multi-main-phase Nd – Ce – Fe – B magnets," *J. Phys. D. Appl. Phys.*, vol. 52, no. 135002, p. 8, 2019.

[83] G. C. Hadjipanayis, G. A. Prinz, and A. Gary, *Science and Technology of Nanostructured Magnetic Materials*. Springer US, 2013.

[84] Liu, J. P., E. Fullerton, O. Gutfleisch, and D. J. Sellmyer, *Nanoscale Magnetic Mateirals and Applications*. Springer US, 2009.

[85] Y. Liu, D. J. Sellmyer, and D. Shindo, *Handbook of Advanced Magnetic Materials*. Springer US, 2006.

[86] J. S. Jiang and S. D. Bader, "Rational design of the exchange-spring permanent magnet," *J. Phys. Condens. Matter*, vol. 26, p. 064214, 2014.

[87] E. Anagnostopoulou, B. Grindi, L. Lacroix, F. Ott, I. Panagiotopoulos, and G. Viau, "Dense arrays of cobalt nanorods as rare-earth free permanent magnets†," *Nanoscale*, vol. 8, pp. 4020–4029, 2016.

감사의 글

더 많은 것을 배우고 알고 싶어 UNIST 에 들어와 대학원생이 된 지도 어느덧 7 년이라는 시간이 흘렀고, 이제는 박사 학위 과정의 끝자락에 서 있습니다. 항상 겸손한 자세로 많은 것을 배우고 발전하려 노력해 왔지만 아직도 부족하기만 합니다. 그럼에도 이 자리에 있을 수 있는 것을 저 혼자만의 힘이라고 생각하지 않습니다. 저를 지도해 주시고 지지해주신 많은 분들 덕분에 무사히 학위를 마칠 수 있었고, 이 글을 통해 감사한 분들에게 작게나마 마음을 표현해 보고자 합니다.

먼저 아무 것도 모르는 저를 거두어 주신 이기석 교수님, 부족하지만 한 명의 연구자로서 성장할 수 있게 앞에서 끌어 주시고 때로는 뒤에서 든든하게 밀어주신 교수님께 진심으로 감사의 말씀을 드립니다. 7 년이라는 짧지 않은 시간을 교수님의 제자로 지내면서 참된 연구자의 자세를 배우고 성장했을 뿐 아니라 인간으로도 많이 성장할 수 있었습니다. 이기석 교수님의 지도와 기다림이 있었기에 지금의 제가 있을 수 있었다고 생각합니다. 그동안의 가르침을 마음에 품고 교수님의 울타리에서 나가서도 항상 정진하여 자랑스러운 제자가 될 수 있도록 노력하겠습니다.

귀중한 시간을 내서 학위 논문 심사를 해 주신 김주영 교수님, 김지윤 교수님, 손흥선 교수님, 박지훈 박사님께도 감사합니다. 저에게 주신 가르침을 새기고 연구하며 살아가도록 하겠습니다. 다양한 학문의 기초를 알려 주신 UNIST 신소재 공학부 교수님들께도 감사의 말씀을 드립니다. 빔라인에 실험하러 갈 때면 실험과 연구 방법에 대해 알려주시고 그 외에도 많은 면에서 도움을 주신 임미영 박사님과 실험하고 있을 때 한번씩 찾아와서 방향을 짚어 주신 유영상 박사님께도 깊은 감사의 말씀을 드립니다.

장비도 제대로 구축되지 않았던 처음의 실험실부터 같이 성장해 나가면서 오랜 시간 함께한 자성 재료 연구실 동료들에게도 늘 감사하고 있다는 말을 전하고 싶습니다. 기쁜 일도 힘든 일도 함께하며 가족보다 긴 시간을 보내온 동료들이 있어서 큰 힘이 되었습니다. 무수한 순간들을 같이 고생하면서 지낸 수석이는 앞으로는 웃는 일만 가득했으면 하고, 항상 열심히 연구하고 연구실에 활력을 불어넣어준 희성이 그리고 함께하며 친동생처럼 지낸 대한이도 부족한 저를 따라주고 끌어줘서 고마웠고 하고자

하는 모든 것이 잘 되기를 진심으로 기원합니다. 분위기를 주도하고 이제는 실험실의 기둥이 된 명환이와 혜진이, 특별히 많은 걸 알려주지 않아도 알아서 잘 하는 강휘, 수영이, 지민이에게도 부족한 선배를 많이 도와줘서 고맙다고 말하고 싶고, 앞으로도 서로 잘 지내고 각자 좋은 결실을 맺었으면 합니다.

항상 뒤에서 응원해주고 격려의 말을 해준 친구들과 지인분들께도 감사의 마음을 전하고 싶습니다.

마지막으로 소중한 가족들에게 감사를 전하고 싶습니다. 언제나 믿음과 사랑으로 저를 대해주신 부모님께 이 기회를 빌려 진심으로 감사하고 사랑한다고 말하고 싶습니다. 부모님의 존중과 신뢰가 있었기에 지금의 제가 있을 수 있었다고 생각합니다. 그리고 하나뿐인 내 동생 남재도 언제나 고맙고 행복 했으면 합니다.

박사라는 가볍지 않은 학위의 무게에 어울리는 사람이 되기 위해, 그리고 수많은 감사한 분들에게 보답하기 위해, 항상 감사하고 불평하지 않으며 “어제의 나보다 나은 나”가 되도록 하겠습니다.

김남규

Curriculum Vitae

Namkyu Kim

School of Materials and Science Engineering
Ulsan National Institute of Science and Technology (UNIST)
UNIST-gil 50, Eonyang-eup, Ulju-gun, Ulsan, 44919, Republic of Korea

Office: 102-dong 705-1-ho
Lab: 102-dong 703-ho
E-mail: kngj@unist.ac.kr
namkyuk88@gmail.com

Education

2016.03 – 2020.02	**Ph.D.** School of Materials and Science Engineering, Ulsan National Institute of Science and Technology (UNIST), Republic of Korea **Thesis Title: Enhancement of Practical Energy Product by Microstructure Modeling** (Advisor: Ki-Suk Lee)
2014.03 – 2016.02	**M.S.** School of Materials and Science Engineering, Ulsan National Institute of Science and Technology (UNIST), Republic of Korea **Thesis Title: Observation of Spin Dynamics Using Atomistic Simulation** (Advisor: Ki-Suk Lee)

2007.03 – 2014.02	**B.S.** School of Advanced Materials Engineering, Chungbuk National University, Republic of Korea (Advisor: Joo Han Kim)

Research interest

1. **Magnetic materials**
2. **Permanent magnet**
   - Rare-earth free magnet
   - Exchange-coupled magnet
3. **Magnet used in motor**

Awards

1	**A Gold Award in the 21st HumanTech Paper Award** – 2018. 2. 11 *Samsung Electronics*
2	**Best Poster Award** – 2018. 07. 26 *International Colloquium on Magnetic Films and Surfaces (ICMFS)*

Publication

___ (underline) indicates **N. Kim**,
* indicates corresponding author

1	M.-S. Jung, M.-Y. Im, B. H. Lee, **N. Kim**, K.-S. Lee*, and J.-I. Hong*, "Magnetism of the hypo-oxide state at the diffuse interface between the ferromagnet and antiferromagnet phases", *Nanoscale* **9**, 14023 (2017).
2	**N. Kim**, H.-S. Han, and K.-S. Lee*, "A Limit to Predict Maximum Energy Product (BH_{max}) from the magnetization Hysteresis Loop", *Journal of the Korean Magnetics Society* **28**(5), 205-211 (2018)
3	S. Lee, H.-S. Han, D.-H. Jung, **N. Kim**, M. Kang, H.-J. Ok, and K.-S. Lee*, "Writing and Deleting Magnetic Bubbles using Local Magnetic Fields", *Journal of Magnetics* **25**(4), 458-462 (2020)
4	**N. Kim**, H.-S. Han, S. Lee, M.-J. Kim, D.-H. Jung, M. Kang, H. Ok, Y. Son, S. Lee*,

	and K.-S. Lee*, "Geometric effects in cylindrical core/shell hard-soft exchange-coupled magnetic nanostructures", *Journal of Magnetism and Magnetic Materials* **523**, 167599 (2021)

Domestic Patents (Registration)

1	K.-S. Lee, H.-S. Han, D.-H. Jung, **N. Kim**, Korea Patent 10-1809242, Spinwave filtering device using magnetic skyrmion (2017) (자기 스커미온을 이용한 스핀파 필터링 소자).
2	K.-S. Lee, D.-H. Jung, H.-S. Han, **N. Kim**, Korea Patent 10-1746698, Skyrmion diode and its operating method (2017) (스커미온 다이오드와 구동 방법)
3	K.-S. Lee, H.-S. Han, D.-H. Jung, **N. Kim**, Korea Patent 10-1825174, Signal transferring device using skyrmion (2018) (스커미온을 이용한 신호 전달 소자)
4	K.-S. Lee, M. Kang, D.-H. Jung, H.-S. Han, S. Lee, **N. Kim**, H.-J. Ok, Korea Patent 10-2147931, METHOD FOR FORMING UNEVENNESS USING MAGNET AND APPARATUS THEREFOR (2020) (자석을 이용한 요철 형성방법 및 요철 형성장치)

International Patent (Application)

1	K.-S. Lee, D.-H. Jung, H.-S. Han, **N. Kim**, U.S. Patent 15/431,488 (2018) SKYRMION DIODE AND METHOD OF MANUFACTURING THE SAME (스커미온 다이오드 및 그 제조 방법).

Presentation (International conferences)

† indicates presenter, ___ (underline) indicates **N. Kim**

1	**N. Kim**†, H.-S. Han, S. Lee, K.-S. Lee, " The Limitation of First Order Reversal Curve Based on Classical Preisach Model", The 11th international conference on advanced materials and devices (ICAMD 2019), Republic of Korea, 10 Dec. (2019)
2	**N. Kim**†, H.-S. Han, S. Lee, K.-S. Lee, "The Practical Energy Product of Cylindrical Core/shell Consist of Soft- and Hard-magnetic Materials", 64th Annual Conference on Magnetism and Magnetic Materials, United States, 05 Nov. (2019)
3	D.-H. Jung†, H.-S. Han, **N. Kim**, K.-S. Lee, "Unidirectional Manipulation of Magnetic Skyrmion Transmission via Asymmetric Modulation of Potential Energy Barrier", 64th Annual Conference on Magnetism and Magnetic Materials, United States, 05 Nov. (2019)
4	**N. Kim**†, H.-S. Han, S. Lee, K.-S. Lee, "The Practical Energy Product of Cylindrical Core/shell Composed of Soft- and Hard-magnetic Materials", 10th Joint European Magnetic Symposia (JEMS 2019), Sweden, 30 Aug. (2019)
5	H.-S. Han, S. Lee, D.-H. Jung, **N. Kim**, K.-S. Lee†, "The three-dimensional nature in magnetic vortex dynamics", 23rd International Colloquium on Magnetic Films and Surfaces (ICMFS-2018), United States, 26 Jul. (2018)
6	**N. Kim**†, H.-S. Han, D.-H. Jung, K.-S. Lee, "Breathing Modes of a Magnetic Skyrmion on a Defective Surface", 23rd International Colloquium on Magnetic Films and Surfaces (ICMFS-2018), United States, 25 Jul. (2018)
7	H.-S. Han†, S. Lee, **N. Kim**, M.-Y. Im, Y.-S. Yu, J.-I. Hong, K.-S. Lee, "Symmetry breaking of 3D flux-closure domain structure", 23rd International Colloquium on Magnetic Films and Surfaces (ICMFS-2018), United States, 24 Jul. (2018)
8	S. Lee†, H.-S. Han, **N. Kim**, M.-Y. Im, J.-I. Hong, K.-S. Lee, "Symmetry Breaking in a Three-Dimensional (3D) Flux-Closure Domain Structure", 21st International Conference on Magnetism (ICM 2018), United States, 19 Jul. (2018)
9	K. Song†, S. Woo, H.-S. Han, M.-S. Jung, M.-Y. Im, K.-S. Lee, P. Fischer, J.-I. Hong, J. W. Choi, B.-C. Min, H. C. Koo, J. Chang, "Nanosecond Skyrmion Dynamics driven by Spin-orbit Torques observed by Time-resolved X-ray Transmission Microscopy", 21st International Conference on Magnetism (ICM 2018), 19 Jul. (2018)
10	**N. Kim**†, H.-S. Han, D.-H. Jung, K.-S. Lee, "Enhancement of the Energy Product in Soft- and Hard-magnetic", 21st International Conference on Magnetism (ICM 2018), United States, 19 Jul. (2018)
11	H.-S. Han†, S. Lee, D.-H. Jung, **N. Kim**, K.-S. Lee, "The Bloch Point Pair-mediated Vortex

	Core Reversal", 21st International Conference on Magnetism (ICM 2018), United States, 17 Jul. (2018)
12	S. Lee, H.-S. Han, **N. Kim**, M.-Y. Im, K.-S. Lee†, "Observation of 3D Magnetic Structure and its Control", The 18th International Symposium on the Physics of Semiconductors and Applications (ISPSA 2018), Republic of Korea, 04 Jul. (2018)
13	**N. Kim**†, H.-S. Han, D.-H. Jung, K.-S. Lee, "Atomistic Simulations on Dynamics of a Magnetic Skyrmion: Role of Atomic Defects in the Breathing Mode", The 18th International Symposium on the Physics of Semiconductors and Applications (ISPSA 2018), Republic of Korea, 03 Jul. (2018)
14	H.-S. Han†, S. Lee, D.-H. Jung, **N. Kim**, K.-S. Lee, "The 3D Spin-wave Modes of the Magnetic Vortex in a Thick Circular Nanodisk", The 5th International Conference of Asian Union of Magnetics Societies (IcAUMS 2018), 07 Jun. (2018)
15	**N. Kim**†, K.-S. Lee, "Micromagnetic Simulations of Magnetization Reversals in Rare-earth Free Permanent Magnets", The 5th International Conference of Asian Union of Magnetics Societies (IcAUMS 2018), Republic of Korea, 05 Jun. (2018)
16	**N. Kim**†, H.-S. Han, D.-H. Jung, K.-S. Lee, "The Effect of Defective Surface on Dynamics of a Magnetic Skyrmion", The 5th International Conference of Asian Union of Magnetics Societies (IcAUMS 2018), Republic of Korea, 04 Jun. (2018)
17	S. Lee†, H.-S. Han, **N. Kim**, M.-Y. Im, J.-I. Hong, K.-S. Lee, "Symmetry Breaking in 3D Magnetic Vortex Core Structure", The 5th International Conference of Asian Union of Magnetics Societies (IcAUMS 2018), Republic of Korea, 04 Jun. (2018)
18	D.-H. Jung†, H.-S. Han, **N. Kim**, K.-S. Lee, "Magnetic Skyrmion Diode: Unidirectional Skyrmion Transport via Confining Potential Modulation", The 5th International Conference of Asian Union of Magnetics Societies (IcAUMS 2018), Republic of Korea, 04 Jun. (2018)
19	D.-H. Jung†, H.-S. Han, **N. Kim**, K.-S. Lee, "Shape of Energy Potentials of the Magnetic Skyrmion in Confined Geometries", 62nd Annual Conference on Magnetism and Magnetic Materials (MMM 2017), United States, 10 Nov. (2017)
20	**N. Kim**†, H.-S. Han, D.-H. Jung, K.-S. Lee, "The Effect of Atomic Defects on Skyrmion Breathing Mode", 62nd Annual Conference on Magnetism and Magnetic Materials (MMM 2017), United States, 09 Nov. (2017)
21	H.-S. Han†, S. Lee, D.-H. Jung, **N. Kim**, K.-S. Lee, "Excitation of novel 3D dynamic modes of a magnetic vortex in a thick circular ferromagnetic nanodisk", 62nd Annual Conference on Magnetism and Magnetic Materials (MMM 2017), United States, 07 Nov. (2017)

Presentation (Domestic conferences)

† indicates presenter, ___ (underline) indicates **N. Kim**

1	S. Lee†, S.-G. Je, H.-S. Han, M. Kang, H.-J. Ok, **N. Kim**, W. Chao, M.-Y. Im, K.-S. Lee, "Study on stochasticity in the switching of Co/Pt nanodisks", The Korean Magnetics Society 2020 Winter Conference, Republic of Korea, 26 Nov. (2020)
2	D.-H. Jung†, H.-S. Han, **N. Kim**, G. Kim, S. Jeong, S. Lee, M.-Y. Im, K.-S. Lee, "Unidirectional Transport of Magnetic Skyrmion through Symmetry-Breaking of Potential Energy Barriers", The Korean Magnetics Society 2020 Winter Conference, Republic of Korea, 26 Nov. (2020)
3	S. Lee†, H.-S. Han, Y.-S. Yu, S.-G. Je, M. Kang, H.-J. Ok, **N. Kim**, W. Chao, M.-Y. Im, K.-S. Lee, "Symmetry breaking in the formation of asymmetric Bloch wall in ferromagnetic dots", The Korean Magnetics Society 2020 Winter Conference, Republic of Korea, 26 Nov. (2020)
4	S. Lee†, H.-S. Han, Y.-S. Yu, S.-G. Je, M. Kang, H.-J. Ok, **N. Kim**, W. Chao, M.-Y. Im, K.-S. Lee, "Controlled Switching of Asymmetric Bloch wall in a Rectangular Ferromagnetic disk", The Korean Magnetics Society 2020 Winter Conference, Republic of Korea, 26 Nov. (2020)
5	D.-H. Jung†, H.-S. Han, **N. Kim**, K.-S. Lee, "Guided Motion of a Magnetic Skyrmion Confined in Spatially Modulated Dzyaloshinskii-Moriya Interaction ", The Korean Magnetics Society 2020 Winter Conference, Republic of Korea, 26 Nov. (2020)
6	**N. Kim**†, H.-S. Han, D.-H. Jung, K.-S. Lee, "Breathing Modes of a Magnetic Skyrmion on a Defective Surface", The Korean Magnetics Society 2020 Winter Conference, Republic of Korea, 26 Nov. (2020)
7	**N. Kim**†, H.-S. Han, D.-H. Jung, K.-S. Lee, "Breathing Modes of a Magnetic Skyrmion on a Defective Surface", The Korean Magnetics Society 2020 Winter Conference, Republic of Korea, 26 Nov. (2020)
8	**N. Kim**†, H.-S. Han, S. Lee, K.-S. Lee, "Structural Control of Demagnetizing Field in the Magnet", The Korean Magnetics Society 2020 Winter Conference, Republic of Korea, 26 Nov. (2020)
9	**N. Kim**†, H.-S. Han, S. Lee, K.-S. Lee, "The Practical Energy Product of Cylindrical Core/shell Consist of Soft- and Hard-magnetic Materials", The Korean Magnetics Society 2020 Winter Conference, Republic of Korea, 26 Nov. (2020)
10	S. Lee†, H.-S. Han, M. Kang, H.-J. Ok, **N. Kim**, M.-Y. Im, K.-S. Lee, "Magnetic Field-induced Switching of Asymmetric Bloch wall in a Ferromagnetic Rectangular disk", The Korean Magnetics Society 2020 Summer Conference, Republic of Korea, 19 Jul. (2020)

11	D.-H. Jung†, H.-S. Han, **N. Kim**, K.-S. Lee, “Manipulation of Magnetic Skyrmion Motion for Unidirectional Transmission by Tuning the Asymmetry of Potential Energy Surfaces", The Korean Magnetics Society 2020 Summer Conference, Republic of Korea, 19 Jul. (2020)
12	D.-H. Jung†, H.-S. Han, **N. Kim**, K.-S. Lee, “Emergent Geometric Confinement of Magnetic Skyrmion by Spatially Modulated Dzyaloshinskii-Moriya Interaction", The Korean Magnetics Society 2020 Summer Conference, Republic of Korea, 19 Jul. (2020)
13	**N. Kim**†, H.-S. Han, S. Lee, K.-S. Lee, “Practical Energy Product of Magnetic Materials", The Korean Magnetics Society 2020 Summer Conference, Republic of Korea, 19 Jul. (2020)
14	**N. Kim**†, H.-S. Han, S. Lee, K.-S. Lee, “Practical Energy Product of Hard- and Soft-magnetic Core/Shell Cylinder", The Korean Magnetics Society 2019 Winter Conference, Republic of Korea, 22 Nov. (2019)
15	**N. Kim**†, H.-S. Han, S. Lee, K.-S. Lee, “The Limitation of Anticipation by First Order Reversal Curve Method", The Korean Magnetics Society 2019 Winter Conference, Republic of Korea, 21 Nov. (2019)
16	H.-S. Han†, S. Lee, D.-H. Jung, S. Jeong, **N. Kim**, K.-S. Lee, "The Vortex Core Switching by Bloch Point Pair", The Korean Magnetics Society 2019 Winter Conference, Republic of Korea, 21 Nov. (2019)
17	D.-H. Jung†, H.-S. Han, **N. Kim**, K. Kim, S. Jeong, K.-S. Lee, "Profile of pontential energy of a geometrically confined skyrmion", The Korean Magnetics Society 2019 Winter Conference, Republic of Korea, 21 Nov. (2019)
18	D.-H. Jung†, H.-S. Han, **N. Kim**, K. Kim, S. Jeong, K.-S. Lee, "Diode-like manipulation of magnetic skyrmion transmission using an asymmetric modification of edge potential energy surface", The Korean Magnetics Society 2019 Winter Conference, Republic of Korea, 21 Nov. (2019)
19	K.-S. Lee†, H.-S. Han, D.-H. Jung, **N. Kim**, "미소자기 전산모사(micromagnetic simulation)의 이해와 실전" The Korean Magnetics Society 2019 Summer Conference, Republic of Korea, 22 May. (2019)
20	**N. Kim**†, H.-S. Han, S. Lee, K.-S. Lee, "The Energy Product of Hard- and Soft- magnetic Cylindrical Core/shell", The Korean Magnetics Society 2019 Summer Conference, Republic of Korea, 22 May. (2019)
21	**N. Kim**†, H.-S. Han, K.-S. Lee, "A Restricted Prediction of Maximum Energy Product from the Magnetic Hysteresis Loop", 2019 Korean Physics Society (KPS) Spring Meeting, Republic of Korea, 25 Apr. (2019)

22	D.-H. Jung†, H.-S. Han, **N. Kim**, K.-S. Lee, "Manipulation of Magnetic Skyrmions Motion in Confined Geometries for Potential Neuromorphic Applications", The Korean Magnetics Society 2018 Winter Conference, Republic of Korea, 23 Nov. (2018)
23	S. Lee†, H.-S. Han, **N. Kim**, M.-Y. Im, J.-I. Hong, K.-S. Lee, "Three-dimensional Magnetic Vortex Structure Transformation", The Korean Magnetics Society 2018 Winter Conference, Republic of Korea, 22 Nov. (2018)
24	H.-S. Han†, D.-H. Jung, S. Lee, **N. Kim**, K.-S. Lee, "Skyrmion manipulation by a rotating current", The Korean Magnetics Society 2018 Winter Conference, Republic of Korea, 22 Nov. (2018)
25	**N. Kim**†, H.-S. Han, D.-H. Jung, K.-S. Lee, "Energy Product Enhancement in Soft-and Hard-magnetic Mixtures", The Korean Magnetics Society 2018 Winter Conference, Republic of Korea, 22 Nov. (2018)
26	**N. Kim**†, H.-S. Han, K.-S. Lee, "A Limited Prediction of Maximum Energy Product from the Magnetization Hysteresis Loop", The Korean Magnetics Society 2018 Winter Conference, Republic of Korea, 22 Nov. (2018)
27	H.-S. Han, S. Lee, D.-H. Jung, **N. Kim**, K.-S. Lee†, "The Three-Dimensional Nature in the Magnetic Vortex dynamics", The Korean Magnetics Society 2018 Spring Conference, Republic of Korea, 30 Mar. (2018)
28	D.-H. Jung†, H.-S. Han, **N. Kim**, K.-S. Lee, "Non-Parabolic Confining Potential Model of Magnetic Skyrmion", The Korean Magnetics Society 2018 Spring Conference, Republic of Korea, 29 Mar. (2018)
29	H.-S. Han†, S. Lee, M.-S. Jung, **N. Kim**, Y.-S. Yu, M.-Y. Im, J.-I. Hong, K.-S. Lee, "The symmetry breaking during a transformation from a vortex core to an asymmetric Bloch wall", The Korean Magnetics Society 2018 Spring Conference, Republic of Korea, 29 Mar. (2018)
30	H.-S. Han†, S. Lee, **N. Kim**, M.-Y. Im, Y.-S. Yu, J.-I. Hong, K.-S. Lee, "Symmetry breaking in 3D flux-closure domain structure", The Korean Magnetics Society 2018 Spring Conference, Republic of Korea, 25 Oct. (2017)
31	K.-S. Lee†, H.-S. Han, S. Lee, **N. Kim**, M.-Y. Im, Y.-S. Yu, J.-I. Hong, "Symmetry Breaking of 3D Flux-Closure Magnetization Configurations in a Circular Disks", The Korean Magnetics Society 2017 Summer Conference, Republic of Korea, 25 May. (2017)
32	H.-S. Han†, S. Lee, D.-H. Jung, **N. Kim**, K.-S. Lee, "Beating modes of a magnetic vortex in thick circular ferromagnetic nanodisks", 2017 Korean Physics Society (KPS) Spring Meeting, Republic of Korea, 20 Apr. (2017)

33	**N. Kim**†, J.-I. Hong, K.-S. Lee, "The spontaneous magnetization enhancement by the thermal fluctuation in a ferro-antiferromagnetic mixed system: an atomistic micromagnetic simulation study", The Korean Magnetics Society 2016 Summer Conference, Republic of Korea, 24 Nov. (2016)